

Hunting Transit Patterns: A Search for Exoplanets Around Ultracool Stars

Master Thesis

Faculty of Science, University of Bern

handed in by

Yanick Schmid

2025

Supervisor

Prof. Dr. Brice-Olivier Demory

Abstract

Potential exoplanet host stars SP1036+1923 (M6.5) and SP0314+1603 (M9), both part of the SPECULOOS target list, were investigated based on single transit-like events detected in ground-based photometric data. A systematic and reproducible workflow is presented for evaluating such events using a combination of TESS and SPECULOOS observations, transit modeling, and variability analysis.

No significant transits were detected in the TESS data for either target. For SP1036+1923, an injection-recovery experiment suggests that a similar transit with a period of ≤ 5 days would be detectable with TESS. The absence of such a signal effectively rules out short-period orbits. A transit model fit to the SAINT-EX light curve constrained the period to $11^{+5.17}_{-4.30}$ days. Additionally, a candidate period of 13.148 days was identified in the SPECULOOS data, aligning with the SAINT-EX event and two other transit-like features. However, these are embedded in broader variability patterns, likely linked to stellar activity, and must therefore be interpreted with caution.

For SP0314+1603, the transit-like signal detected with the EUROPA telescope is not recoverable in the TESS data. An MCMC fit constrains the orbital period to $21.57^{+15.94}_{-9.55}$ days, with periods ≤ 5 days ruled out. The SPECULOOS light curves show strong stellar variability, consistent with the targets late spectral type. Initial modeling with a sine function and autocorrelation analysis (ACF) revealed non-stationary, quasi-periodic behavior. A composite Gaussian Process kernel (SHO and Matern) was used to model this variability. In the GP residuals, 13 potentially transit-like features were visually identified. A candidate period of 21.3 days matched four of these patterns and produced a consistent dip in the phase-folded light curve, though notably shallower than the initial event. However, variations in transit shape and timing, as well as the potential influence of residual variability or systematics, limit the confidence in this interpretation.

While a planetary origin remains uncertain for both targets, the analysis provides a strong motivation for continued follow-up. This work highlights the challenges of transit detection in highly variable stars and the need for sophisticated modeling techniques in the presence of correlated noise.

Contents

1	Introduction	1
1.1	The Transit Method	1
1.1.1	Transit Model	2
1.2	Ground-Based Projects	3
1.3	TESS	3
1.4	Ultracool Dwarfs	3
2	Statistical Methods	5
2.1	Box Least Square Algorithm	5
2.2	Lomb-Scargle periodogram	5
2.3	Auto-Correlation Function	6
2.4	Markov Chain Monte Carlo	6
2.5	Gaussian Process	7
3	SP1036+1923: Light Curve Analysis	9
3.1	Initial Transit Candidate	9
3.2	TESS Photometry	11
3.2.1	Injection-Recovery Analysis	13
3.3	MCMC Fit of the Transit Candidate	15
3.4	Inspection of SPECULOOS Data	19
3.5	Discussion	21
4	SP0314+1603: Light Curve Analysis	22
4.1	Initial Transit Candidate	22
4.2	TESS Photometry	23
4.2.1	Injection-Recovery Analysis	24
4.3	MCMC Fit of the Transit Candidate	25
4.4	Modeling of Stellar Variability	29
4.4.1	Data Reduction	29
4.4.2	Initial Steps and Diagnostics	30
4.4.3	Sinusoidal Modeling of Stellar Variability	32
4.5	Gaussian Process	36
4.5.1	Refining Hyperparameters Using Injected Transits	40
4.5.2	Optimized GP Model	40
4.5.3	BLS on Residual Flux	43
4.5.4	Visual Inspection of Residual Flux	44
4.5.5	Folded Light Curve	45
4.5.6	Discussion and Limitations of This Approach	48
4.5.7	Outlook	49
5	Sp0720-0846 - Scholz's Star	50
6	Conclusion and Outlook	51

A TESS analysis of SP1036+1923	57
B Python Code Setup for GP Modeling	58
C Transit-Like Residuals Inspection	59

1 Introduction

The field of exoplanetary science is highly active and has become one of the key areas in modern astronomical research. Exoplanets are planets that orbit a star other than our Sun. The detection of the first exoplanet around a main-sequence star by Michel Mayor and Didier Queloz in 1995 ([Mayor & Queloz, 1995](#)) marked the beginning of a new era in astronomy. Space-based missions such as *Kepler* ([Borucki et al., 2010](#)) and *TESS* ([Ricker et al., 2015](#)) along with ground-based surveys have significantly advanced the field. As of today, there have been over 5,800 confirmed exoplanets¹. Detecting transiting exoplanets is the first step in identifying potentially habitable worlds. It allows for follow-up studies with cutting-edge instruments like the James Webb Space Telescope (JWST, [Gardner et al. \(2006\)](#)) to analyze atmospheric compositions and search for bio-signature gases ([Seager et al., 2015](#)). Moreover, exoplanet discoveries provide insights into planetary system architectures, refine theories of planet formation, and improve our understanding of interactions between planets and their host stars.

Exoplanets vary widely in size and composition, ranging from terrestrial planets (rocky planets comparable in size to Earth) to gas giants as massive as or larger than Jupiter ([Winn & Fabrycky, 2015](#)). In the search for potentially habitable planets, cool stars have proven to be promising, with the TRAPPIST-1 system ([Gillon et al., 2017](#)) serving as a prime example.

Various methods exist for detecting and characterizing exoplanets. The first exoplanet was discovered using the radial velocity (RV) method, which measures periodic shifts in the spectral lines of a star caused by the gravitational pull of an orbiting planet. This Doppler shift in the star's light reveals the presence of an unseen companion ([Mayor & Queloz, 1995](#)). Another frequently used detection technique is Direct Imaging. Here, images of exoplanets are captured by blocking out starlight to reveal faint planetary companions. The HR 8799 system, which revealed three orbiting planets, is a landmark example ([Marois et al., 2008](#)).

However, the most successful method in terms of number of detections is the transit method, which is also the technique used in this thesis.

1.1 The Transit Method

The transit method (e.g., [Winn \(2010\)](#)) relies on the observation of a star's brightness over time. When a planet crosses in front of its host star (as seen from Earth), it temporarily blocks a small fraction of the starlight, causing a periodic dip in the star's observed brightness. This dip, known as a transit, is recorded in a light curve, a time series of photometric measurements. For a transit to be observable, the orbital plane of the exoplanet must be aligned nearly edge-on with respect to the observer's line of sight. The probability of an exoplanetary system exhibiting transits is given by:

$$P_{\text{transit}} = \frac{R_{\text{star}} + R_{\text{planet}}}{a}, \quad (1)$$

where R_{star} is the stellar radius, R_{planet} is the planetary radius and a is the semi-major axis of the planet's orbit.

In the Solar System, the probability of observing transits of inner planets such as Venus and Mercury from a random vantage point in space is less than one percent. However, planets with short orbital periods and large radii are more likely to transit and produce deeper dips in their host stars light curve, making them easier to detect. The transit depth δ (reduction in the observed brightness of star during a transit) provides information about the radius ratio between the star and the planet:

¹https://exoplanetarchive.ipac.caltech.edu/docs/counts_detail.html (accessed April 1, 2025).

$$\delta = \frac{R_{\text{planet}}^2}{R_{\text{star}}^2}, \quad (2)$$

From a transit light curve, parameters can be derived, including transit depth (δ), transit duration (total time the planet spends crossing the star), ingress/egress duration (time for the planet to fully enter or exit transit) and the orbital period (time between consecutive transits). An important concept that influences the transit shape is limb-darkening. It refers to the decrease in intensity on the stellar disk (from the line of sight) from center to the edges. This effect causes the ingress and egress of a transit to appear gradual rather than abrupt.

1.1.1 Transit Model

The shape of a transit is determined by the geometry and properties of the planet-star system. As such, it is possible to infer key system parameters from the observed light curve. Analytical transit models describe the relationships between these parameters. In this thesis, we model transits using the `batman` package (Kreidberg, 2015), which implements the analytical transit model of Mandel & Agol (2002). The transit model used in this thesis is defined by the following parameters: mid-transit time (t_0), orbital period (P), planet-to-star radius ratio (R_p/R_\star), impact parameter (b), stellar density (ρ_\star) and the quadratic limb-darkening parameters u_1 and u_2 .

The semi-major axis in units of stellar radii (a/R_\star) can be computed via Kepler's Third Law under the assumption of a circular orbit:

$$a/R_\star = \left(\frac{G\rho_\star P^2}{3\pi} \right)^{1/3}, \quad (3)$$

where G is the gravitational constant.

The impact parameter b describes how centrally the planet crosses the stellar disk, based on the projected distance from the center of the star during transit. This value affects the shape of the light curve: a low b means the planet crosses near the center of the star, producing a more U-shaped transit, while a high b corresponds to a grazing transit near the edge of the star, often resulting in a more V-shaped light curve. The orbital inclination i is derived from the relationship between the impact parameter b and a/R_\star :

$$i = \arccos \left(\frac{b}{a/R_\star} \right). \quad (4)$$

The transit duration can be calculated via

$$T_{\text{dur}} = \frac{P}{\pi} \frac{\sqrt{(1+R_p/R_\star)^2 - b^2}}{a/R_\star}. \quad (5)$$

We adopt the commonly used quadratic limb-darkening law:

$$I(\mu) = 1 - u_1(1 - \mu) - u_2(1 - \mu)^2,$$

where $\mu = \cos \theta$ is the angle between the star's surface normal and line of sight and parameters u_1 and u_2 are the quadratic limb-darkening coefficients, inferred from stellar models (Mandel & Agol, 2002; Parviainen & Aigrain, 2015).

1.2 Ground-Based Projects

Ground-based facilities such as the SPECULOOS project (Delrez et al., 2018) or the SAINT-EX telescope (Gómez Maqueo Chew et al., 2023) significantly contribute to the field by observing small planets around ultracool dwarfs. They complement space-based missions by providing high-precision photometric monitoring.

SPECULOOS (Search for habitable Planets EClipsing ULtra-cOOl Stars) (Delrez et al., 2018) is an international network of 1-meter robotic telescopes. It consists of the SPECULOOS Southern Observatory (SSO) at Paranal Observatory, Chile, with four telescope and the SPECULOOS Northern Observatory (SNO) at the Teide Observatory, Tenerife. The project targets approximately 1200 bright ultracool dwarfs in the infrared, aiming to detect transiting Earth-sized planets around them (Sebastian et al., 2021).

The SAINT-EX (Search And characterIsatioN of Transiting EXoplanets) telescope (Gómez Maqueo Chew et al., 2023), located in San Pedro Martir in California, Mexico, has a similar design to the SSO telescopes. It is a 1-meter Ritchey-Chrtien telescope with an Andor Ikon CCD. The telescope is equipped with a Sloan *ugriz'* filter set and has a field of view of 12'12'. SAINT-EX supports the SPECULOOS network and specializes in high-precision near-infrared time-series photometry, making it particularly well-suited for detecting transits of planets around ultracool stars. Photometric data is generated from SAINT-EX observations by processing the raw science frames and calibrated images using *PRINCE* pipeline (Photometric Reduction and In-depth Nightly Curve Exploration, (Demory et al., 2020)), which applies bias, dark, and flat-field corrections. The world coordinate system (WCS) is derived using Astrometry.net (Lang et al., 2010), and potential reference stars are identified via Photutils star detection (Bradley et al., 2024). Stars are selected for differential photometry if their peak flux exceeds the background level by a threshold scaled to the median nightly noise. The pipeline then performs aperture and annulus photometry for each exposure and corrects for systematics using a Principal Component Analysis approach (Pedregosa et al., 2011). For a detailed introduction to CCD astronomy, we refer to Howell (2006).

1.3 TESS

NASAs Transiting Exoplanet Survey Satellite (Ricker et al., 2015) is a space-based mission dedicated to detecting transiting exoplanets around bright, nearby stars. It complements ground-based surveys by covering a wide field and identifying candidates for follow-up characterization with instruments such as SPECULOOS, SAINT-EX, and JWST. During the two-year primary mission (2018-2020), TESS monitored approximately 85% of the sky, each sector for about 27 days. The extended mission (2020-2022) revisited much of the sky, including the northern ecliptic hemisphere, with improved observing cadence (Bell, 2020). TESS achieves high photometric precision, allowing the detection of small planets around bright stars. All data products of TESS are publicly available. As of 2025, TESS has identified over 7,500 planet candidates and confirmed more than 600 planets².

1.4 Ultracool Dwarfs

Ultracool dwarfs (UCDs) are the primary targets of the SPECULOOS project (Sebastian et al., 2021). These objects are classically defined by temperatures below 2700K, and include both low-mass stars and brown dwarfs (substellar objects that lack sufficient mass for sustained hydrogen fusion). Their spectral types range from M7 to T6.5, and their peak emission falls in the near- and mid-infrared (Davy Kirkpatrick et al., 2012; Cushing et al., 2011).

²<https://exoplanetarchive.ipac.caltech.edu/>, visited on 01.04.2025

One of the key advantages of observing UCDs for transits is their small radii. According to Equation (2), the transit depth of an Earth-sized planet is about two orders of magnitude greater around a UCD compared to a Sun-like star, significantly improving detectability. Additionally, their habitable zones are much closer to the star, increasing the probability of observing transits (Equation 1).

A well-studied example for planets around UCD is the already mentioned TRAPPIST-1 system, which hosts seven Earth-sized planets, three of them in the habitable zone (Gillon et al., 2017). This system exemplifies why UCDs are prime targets for transit searches. Models suggest that Earth-sized planets are common around UCDs (Payne & Lodato, 2007). The planetary population of UCDs is however still largely unexplored, motivating continued observations.

Ultracool dwarfs within 20 parsecs have been cataloged through different surveys, e.g., the Two Micron All Sky Survey (Skrutskie et al., 2006), or the Sloan Digital Sky Survey (York et al., 2000).

Ultracool dwarfs often exhibit large photometric variability. This can be due to rotational modulation of features such as differential rotation (different parts of the object moving with different velocities), atmospheric dynamics or evolving clouds. As the object rotates, different regions rotate into and out of view, they can produce quasi-periodic modulations in the observed flux. However, the evolving nature of these clouds can cause the periodicity to vary or decay over time. Observations of systems like Luhman 16 (a brown dwarf binary) have revealed fast-evolving weather patterns, underlining the highly variable nature of brown dwarf atmospheres (Street et al., 2015; Gillon et al., 2013). These atmospheric dynamics manifest in light curves as quasi-periodic or evolving variability, which can complicate the detection and interpretation of transit signals (Petrucci et al., 2024).

2 Statistical Methods

In this section an overview is provided of the statistical methods employed in the analysis of light curves for the detection and characterization of exoplanetary transits.

2.1 Box Least Square Algorithm

The Box Least Square (BLS) algorithm (Kovács et al., 2002) is a classical tool for the detection of periodic transits in photometric time-series data. It models transits as box-shaped features, characterized by two distinct flux levels: the out-of-transit baseline flux H and the in-transit flux L , where the difference ($H - L$) defines the transit depth. The model further depends on three key parameters: the transit duration, the mid-transit time and the orbital period. Under the assumption that measurements uncertainties are independent and normally distributed, the BLS algorithm computes the maximum likelihood fit of a box-shaped transit model to the observed light curve. It is maximized across a grid of trial periods, durations, and phase offsets, identifying the combination that best explains the observed flux variations. The BLS periodogram thus provides a statistical measure of transit likelihood across the tested parameter space, with significant peaks indicating strong candidate signals. Due to its computational efficiency and sensitivity, BLS has become a standard tool in exoplanet surveys such as Kepler and TESS. However, its reliance on a box-shaped model makes it less suited for detecting signals with complex shapes (e.g., grazing eclipses or prominent stellar variability). In the present work, we use the implemented *BoxLeastSquares* class in *Astropy* (Astropy Collaboration et al., 2022) to perform BLS analysis.

To assess the significance of a detected signal, we employ the Signal Detection Efficiency (SDE) metric following the approach of Hippke & Heller (2019). The SDE is based on the Signal Residue (SR), which quantifies the relative goodness-of-fit of transit models across trial periods P :

$$\text{SR}(P) = \frac{\chi_{\min, \text{global}}^2}{\chi_{\min}^2(P)}, \quad (6)$$

where $\chi_{\min}^2(P)$ is the minimum chi-squared value for a transit model at period P , and $\chi_{\min, \text{global}}^2$ is the global minimum across all periods. This formulation ensures that $\text{SR}(P) \leq 1$, with values closer to 1 indicating a better fit relative to the global best. The SDE is then computed as:

$$\text{SDE} = \frac{\text{SR}_{\text{peak}} - \langle \text{SR} \rangle}{\sigma(\text{SR})}, \quad (7)$$

where SR_{peak} is the maximum SR value, $\langle \text{SR} \rangle$ is the mean, and $\sigma(\text{SR})$ is the standard deviation across all trial periods. Following Hippke & Heller (2019), we adopt a detection threshold of $\text{SDE} > 7$ to indicate a statistically significant detection.

2.2 Lomb-Scargle periodogram

The Lomb-Scargle periodogram (Lomb, 1976; Scargle, 1982) is a modification of the Fourier transform adapted for unevenly sampled time-series data. This routine fits sinusoidal functions at multiple test frequencies, computing a normalized power spectrum. High power values indicate frequencies where a sinusoidal model provides a good fit, suggesting the presence of a periodic signal. The Lomb-Scargle method is particularly useful for detecting quasi-periodic signals (e.g., stellar rotation, pulsations) and has been widely applied in time-domain astronomy (VanderPlas, 2018). Lomb-Scargle periodograms are computed using the built-in function *LombScargle* from *Astropy* (Astropy Collaboration et al., 2022).

2.3 Auto-Correlation Function

Complementary to periodogram-based approaches, the Auto-Correlation Function (ACF) provides a model-independent measure of periodicity by quantifying the self-similarity of a light curve at different time lags τ . The ACF is defined as (see, e.g., ([Shumway & Stoffer, 2020](#))):

$$ACF(\tau) = \frac{\sum_{t=1}^{N-\tau} (y_t - \bar{y})(y_{t+\tau} - \bar{y})}{\sum_{t=1}^N (y_t - \bar{y})^2}, \quad (8)$$

Where N is the total number of observations, \bar{y} is the sample mean, and y_t represents the measured value at time t .

For a strictly periodic signal with period P , the ACF exhibits peaks at lags $\tau = nP$ (where n is an integer), with the primary peak at $\tau = P$ indicating the dominant period. Unlike BLS or Lomb-Scargle, the ACF does not assume a specific signal shape, making it robust against non-sinusoidal variability. The ACF is particularly effective in detecting stellar rotation periods in photometric data, even in the presence of noise and instrumental systematics ([McQuillan et al., 2013](#)). We analyze time-series correlations using the ACF implemented in *StatsModels* ([Seabold & Perktold, 2010](#)).

2.4 Markov Chain Monte Carlo

Markov Chain Monte Carlo (MCMC) algorithms are a powerful class of methods for sampling probability distributions. The MCMC approach provides a robust way to infer most probable parameters of a model given the data. For theoretical background on MCMC, see [Gelman et al. \(2013\)](#) or [Hastings \(1970\)](#).

MCMC operates within a Bayesian statistical framework, which relates the posterior distribution of parameters to the likelihood of the data and prior knowledge. This approach is grounded in Bayes' theorem:

$$P(\theta|D) = \frac{P(D|\theta)P(\theta)}{P(D)}, \quad (9)$$

where $P(\theta|D)$ is the posterior distribution of parameters θ given data D , $P(D|\theta)$ is the likelihood, which expresses how likely the observed data are given the model parameters, $P(\theta)$ represents prior knowledge about the parameters, and $P(D)$ serves as a normalization constant. In practice, computing $P(D)$ (the *marginal likelihood* or *Bayesian evidence*) is often computationally intractable, but since it does not depend on θ , we can work with the proportionality:

$$P(\theta|D) \propto P(D|\theta)P(\theta). \quad (10)$$

MCMC algorithms efficiently sample from this posterior distribution by constructing a Markov chain whose stationary distribution converges to $P(\theta|D)$. Prior knowledge can be incorporated through prior distributions, which guide the sampling process. A uniform prior $\mathcal{U}(x, y)$ allows for sampling with equal probability within the range $[x, y]$. A Gaussian prior $\mathcal{N}(\mu, \sigma)$ encourages sampling around the mean μ , with a standard deviation σ .

The MCMC algorithm generates a sequence of parameter values $\{\theta_i\}$, though a random walk in parameter space. At each step, a new set of parameters is proposed and either accepted or rejected, based on the implemented criterion. This ensures that the chain eventually samples from the true posterior distribution.

The MCMC algorithm is particularly useful for fitting transit models to light curve data, as it enables sampling of the parameter space and provides statistically meaningful posterior distributions. When the algorithm converges properly, it yields reliable estimates for the transit parameters introduced in Section 1.1.

In this work, we use the *emcee* Python package (Foreman-Mackey et al., 2013), an implementation of Goodman and Weares Affine-Invariant MCMC Ensemble Sampler (Goodman & Weare, 2010). It is well-suited for efficiently exploring parameter space and improving convergence in Bayesian inference.

2.5 Gaussian Process

Gaussian Processes (GPs) are a powerful tool for modeling data. They provide a flexible, non-parametric framework for modeling stochastic processes by generalizing Gaussian distributions to function spaces. Unlike parametric approaches, a GP defines a probability distribution over all possible functions consistent with observed data, making it particularly valuable for modeling complex variability and systematics in astronomical time series (see e.g., Aigrain et al. (2016)). For a detailed introduction to Gaussian Processes, see Rasmussen & Williams (2006).

A GP is fully specified by its mean function $\mu(x)$ and covariance kernel $k(x, x')$:

$$f(x) \sim \mathcal{GP}(\mu(x), k(x, x')). \quad (11)$$

For any finite set of inputs $X = \{x_1, \dots, x_n\}$, the corresponding function values

$$f(X) = \{f(x_1), f(x_2), \dots, f(x_n)\} \quad (12)$$

follow a multivariate normal distribution

$$f(X) \sim \mathcal{N}(\mu, \mathbf{K}), \quad (13)$$

where $\mathbf{K}_{ij} = k(x_i, x_j)$ is the covariance matrix, encoding correlations between function values at different points. A common assumption is that $\mu(x) = 0$, in which case the covariance function fully determines the behavior of the GP.

The covariance kernel plays a crucial role in shaping the functional behavior of the model. The kernel is controlled by hyperparameters θ that define the correlation structure of function values. The simplest example is the constant kernel:

$$k(x_i, x_j) = C, \quad (14)$$

which assumes that all function values are equally correlated, resulting in a constant function with Gaussian noise. The only hyperparameter in this case is the constant C , which controls the scale of the function values.

A more sophisticated choice is the Simple Harmonic Oscillator (SHO) kernel, designed to model (quasi-)periodic signals with damping. It is particularly useful for modeling stellar variability and correlated noise in light curves. The covariance function in the frequency domain (power spectral density) is given by:

$$S(\omega) = \sqrt{\frac{2}{\pi}} \frac{S_0 \omega_0^4}{(\omega^2 - \omega_0^2)^2 + \frac{\omega^2 \omega_0^2}{Q^2}}, \quad (15)$$

where $\omega = 2\pi f$ is the angular frequency. The hyperparameters of this kernel are:

- S_0 : The amplitude scaling factor, determining the overall signal strength.
- ω_0 : The characteristic frequency, related to the period $P_0 = \frac{2\pi}{\omega_0}$.

- Q : The quality factor, which measures the damping of oscillations, $Q = \frac{\omega_0}{2\gamma}$, where γ is the damping coefficient. Higher Q values correspond to long-lived oscillations, while lower values indicate more irregular variations.

Another widely used covariance function for GP modeling is the Matern kernel. It is particularly suited for processes with varying degrees of smoothness. It generalizes the squared exponential kernel (SE) by introducing a smoothness, ν , which controls whether the function is highly differentiable or exhibits a rough, jagged structure. The Matern covariance function is given by:

$$k_\nu(r) = \sigma^2 \frac{2^{1-\nu}}{\Gamma(\nu)} \left(\frac{\sqrt{2\nu}r}{\rho} \right)^\nu K_\nu \left(\frac{\sqrt{2\nu}r}{\rho} \right), \quad (16)$$

where:

- σ : Amplitude of the Gaussian Process.
- $r = |t - t'|$: Time separation between two observations.
- ρ : Characteristic length scale, controlling how quickly correlations decay.
- ν : Smoothness parameter, determining function differentiability.
- K_ν : modified Bessel function of the second kind.
- $\Gamma(\nu)$: Gamma function.

The kernel has three hyperparameters: σ , ν and ρ . As $\nu \rightarrow \infty$, the Matern kernel converges to the SE kernel, producing infinitely differentiable functions. In this work, we use the *celerite* package ([Foreman-Mackey et al., 2017](#)), which implements a Matern $\nu = \frac{3}{2}$ kernel for efficient Gaussian Process modeling, ensuring moderate smoothness.

A key advantage of GPs is their ability to handle irregularly sampled data and interpolate over gaps. The covariance function ensures that predictions in missing regions remain consistent with observed data. When observations are sparse, the uncertainty increases. When data is dense, the GP prediction aligns closely with observed values. If the kernel has a long correlation length, the GP will smoothly extrapolate through gaps.

3 SP1036+1923: Light Curve Analysis

SP1036+1923 is an M6.5 dwarf at a distance of 17.3 parsec, with an effective temperature of $T_{\text{eff}} = 2850\text{K}$. It is part of the SPECULOOS target list [Sebastian et al. \(2021\)](#). The fundamental properties of the star including astrometric position, spectral classification, and photometric magnitudes are summarized in Table 1.

Table 1: Fundamental parameters of the target star SP1036+1923.

Parameter	Value
ICRS Coordinates (J2000)	10:36:08.7158 +19:23:30.6509
Spectral Type	M6.5
<i>G</i> -band magnitude	15.1
<i>J</i> -band magnitude	11.3
<i>K</i> -band magnitude	10.3
Stellar Radius	$0.137 \pm 0.02 R_{\odot}$
Stellar Mass	$0.111 \pm 0.001 M_{\odot}$
Effective Temperature (T_{eff})	2850 K
Surface Gravity ($\log g$)	4.72

The stellar parameters T_{eff} and surface gravity ($\log g$) were derived from spectroscopic observations of ultracool dwarfs in LAMOST DR7 by [Wang et al. \(2022\)](#). SP1036+1923 is a dense, low-mass main-sequence star.

3.1 Initial Transit Candidate

In the early stages of this project, an intriguing pattern was identified in the light curve of SP1036+1923, observed with the SAINT-EX telescope. The automatic reduction pipeline *PRINCE* (see section 1.2) processes each observation night, producing light curves along with relevant metadata on targets and reference stars. The report for March 13, 2024, contained the light curve shown in Figure 1.

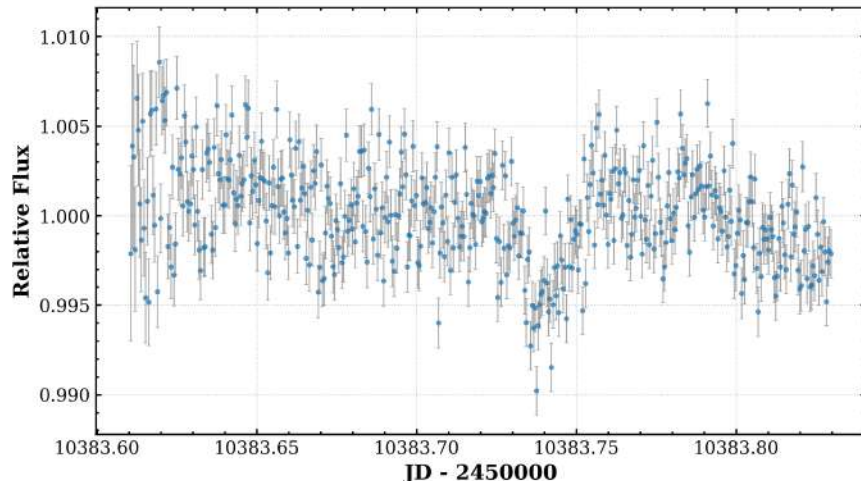


Figure 1: Light Curve of Sp1036+1923 from the night of 2024-03-13.

A distinct decrease in flux is visible between 10383.725 and 10383.76 (BJD). The exposure time for this observation was 35 seconds and it was observed in the I+z filter. To assess potential systematic influences, key observational parameters are shown in Figure 2.

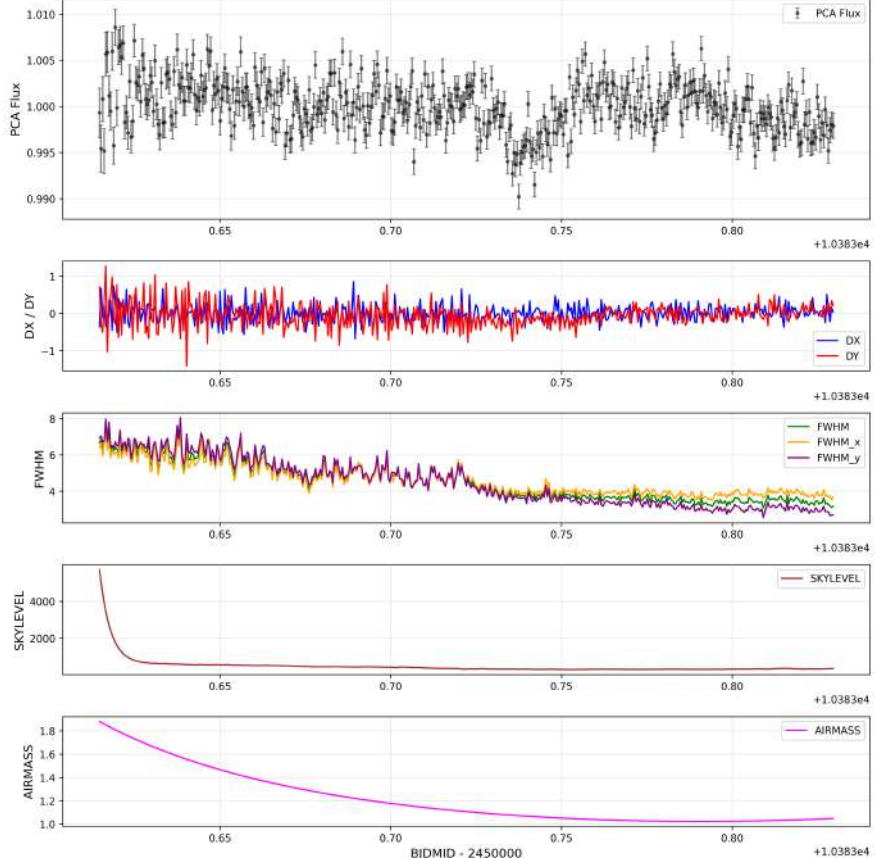


Figure 2: Systematic parameters of the observation of Sp1036+1923.

The second row of Figure 2 displays DX and DY , the positional shifts of the target star on the detector in x- and y- directions. Significant shifts can cause changes in the measured flux. However, no significant displacement coincides with the observed dip. Similarly, SKYLEVEL (background sky brightness) and AIRMASS (atmospheric path length, normalized to 1 at zenith) remain stable during the event. The Full Width at Half Maximum ($FWHM$), which quantifies the spatial extent of the star's point spread function (PSF), does show a slight reduction around the beginning of the flux dip. This could indicate changes in atmospheric seeing, focus drift, or minor telescope tracking errors. However, the magnitude of this change is insufficient to account for the observed signal. Additionally, systematic detrending with respect to $FWHM$ did not significantly alter the shape of the dip, let alone remove it entirely.

To further evaluate the origin of this feature, the data reduction was manually repeated using independent detrending techniques, including processing using AstroImageJ (Collins et al., 2016). Additional environmental parameters such as humidity were also checked. The signal remained consistent across different reduction methods and when using an alternative set of reference stars. Given the robustness of this feature, we conclude that the dip is genuine and is astrophysical in nature. To investigate the possibility of it being a planetary transit, we turn to further analysis to identify similar events and constrain system parameters.

3.2 TESS Photometry

TESS observed SP1036+1923 across multiple sectors (22, 45, 46, 48, 72), with varying exposure times (120s, 200s, 600s and 1800s). The data were retrieved using the *lightkurve* Python package ([Lightkurve Collaboration et al., 2018](#)), with outliers and NaNs removed.

The raw light curve may contain low-frequency variability that can obscure transit signals. After detrending, periodic variations due to potential transits become clearer. To mitigate these systematics, we applied a Savitzky-Golay filter, optimizing the window length by minimizing the Combined Differential Photometric Precision (CDPP) as defined by [Koch et al. \(2010\)](#). Importantly, the window length was chosen to be long enough to preserve variability on timescales of 50 minutes, ensuring that any potential transit signal corresponding to the signal in Figure 1 remained unaffected. Also, it was attempted to maximize the SDE. Figure 3 shows the 120s exposure dataset before and after detrending.

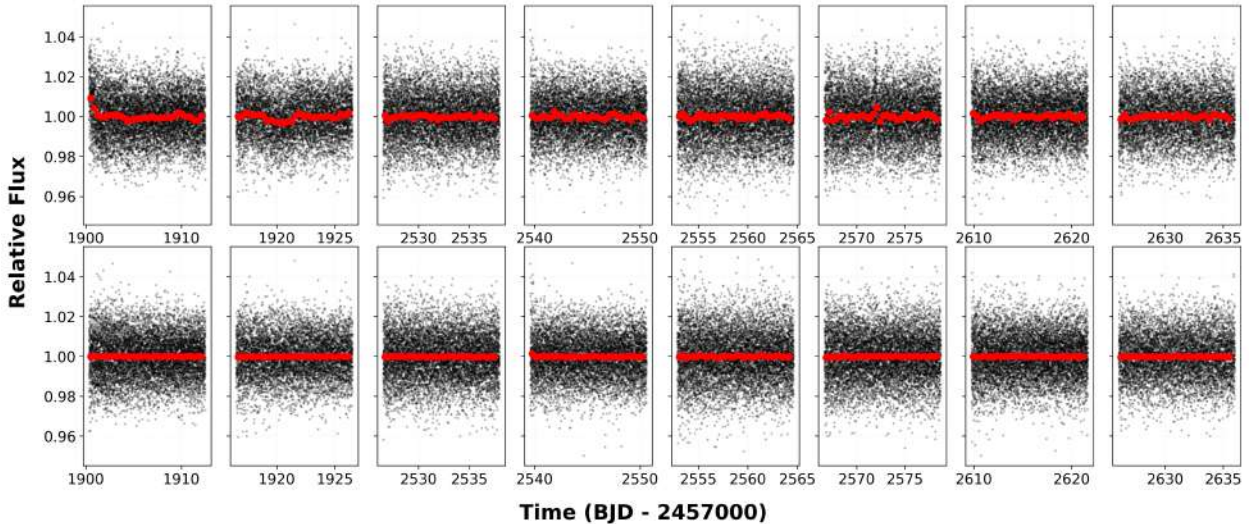


Figure 3: TESS light curve for SP1036+1923 before (top) and after (bottom) detrending. The raw flux (top) and detrended flux (bottom) are shown with individual data points (black) and binned points (red). The Savitzky-Golay filter was applied with an optimal window length of 101 data points.

This detrending approach was applied to all available exposure times. While longer exposures (600s and 1800s) are useful for other studies, they are poorly suited for detecting 50-minute transits, providing only about 5 and 2 data points per transit respectively.

The BLS analysis of the 120s cadence data identified a periodic signal with a period of 20.36 days (see Figure 4), showing a transit duration of 1.20 hours and depth of 4.17 ppt. However, these transit parameters do not match the characteristics of the initial transit candidate (see Figure 1). Moreover the corresponding ephemeris also does not align with the timing of that event. To assess the significance of this detection in the BLS periodogram, we employed the Signal Detection Efficiency (SDE; see Section 2.1). The calculated SDE of 5.78 falls below the adopted threshold for reliable transit detection of SDE = 7. Combined with the mismatch in transit properties, we conclude that this signal is likely a statistical fluctuation rather than a robust planetary transit.

Table 2 summarizes the BLS parameters for all exposure times. The analysis yielded no significant detections (SDE < 7.0 for all cases), and none of the ephemeris matched the transit candidate observed with SAINT-EX, even when considering generous timing uncertainties. We tested multiple period grids and ranges in our BLS searches, but none produced a significant detection. The corresponding BLS periodograms

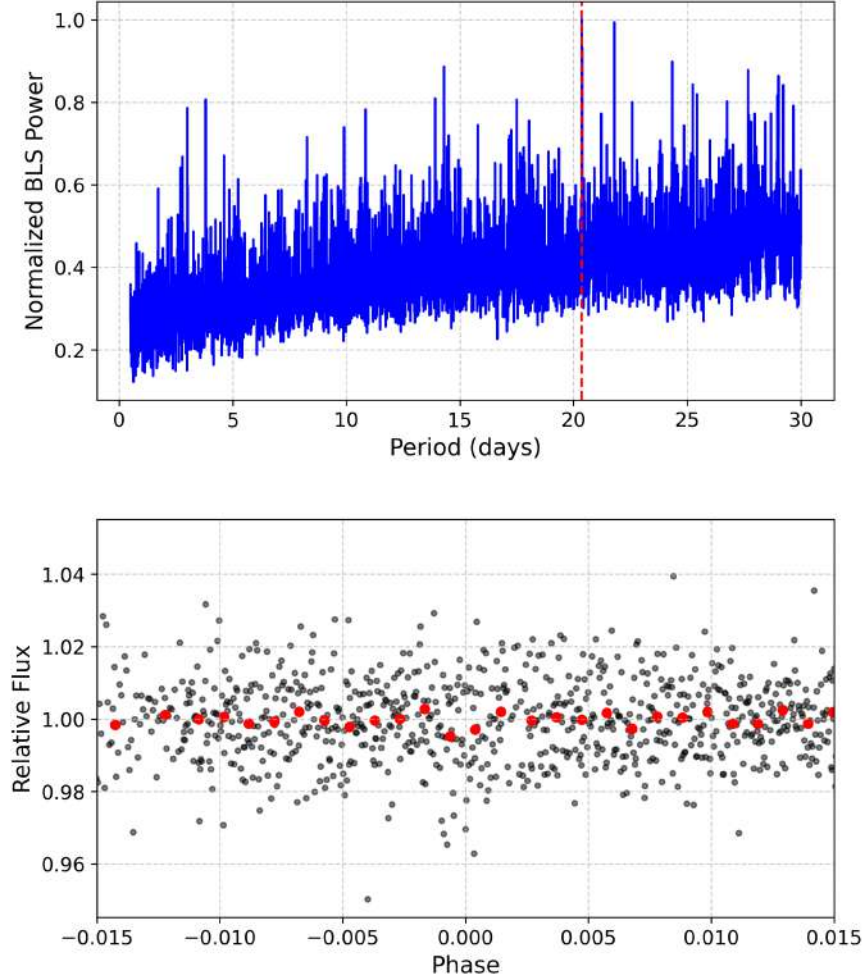


Figure 4: TESS data of SP1036+1923: Analysis of the 120s cadence data showing (top) the BLS periodogram with peak power at 20.36 days (red dashed line), and (bottom) the phase-folded light curve centered on the candidate transit. The phase-folded plot shows the relative flux variations binned in red over the original data points in black, with the x-axis focused on the putative transit window.

are in Appendix A.

Table 2: Best-fit BLS Transit Parameters for Different Exposure Times. The results are based on a Box Least Squares (BLS) periodogram analysis. The SAINT-EX row is included for comparison with an independently determined transit event.

Exposure Time (s)	Period (days)	Duration (days)	Depth	t_0 (BJD - 2457000)
200	13.26	0.1	0.024	3261.36970
600	19.885	0.1	0.00716	2525.54114
1800	14.30	0.2	0.0081	1899.47393
SAINT-EX	—	0.035	0.0045	3383.7425

3.2.1 Injection-Recovery Analysis

To validate and illustrate the performance of our transit detection approach, an injection-recovery experiment was performed using TESS data (120 s cadence). We start with a simple approach to visualize different scenarios of transits in the TESS data before turning to a broader, more systematic approach.

We injected synthetic, box-shaped transits with a depth of 0.45% and a duration of 0.035 days into the TESS light curve, based on the approximate characteristics of the initial transit candidate. Transits were injected at three orbital periods: 5, 10, and 15.5 days. The results are summarized in Figure 5. The top row shows the BLS periodograms for each injected case, while the bottom row shows the corresponding phase-folded light curves centered on the detected signals.

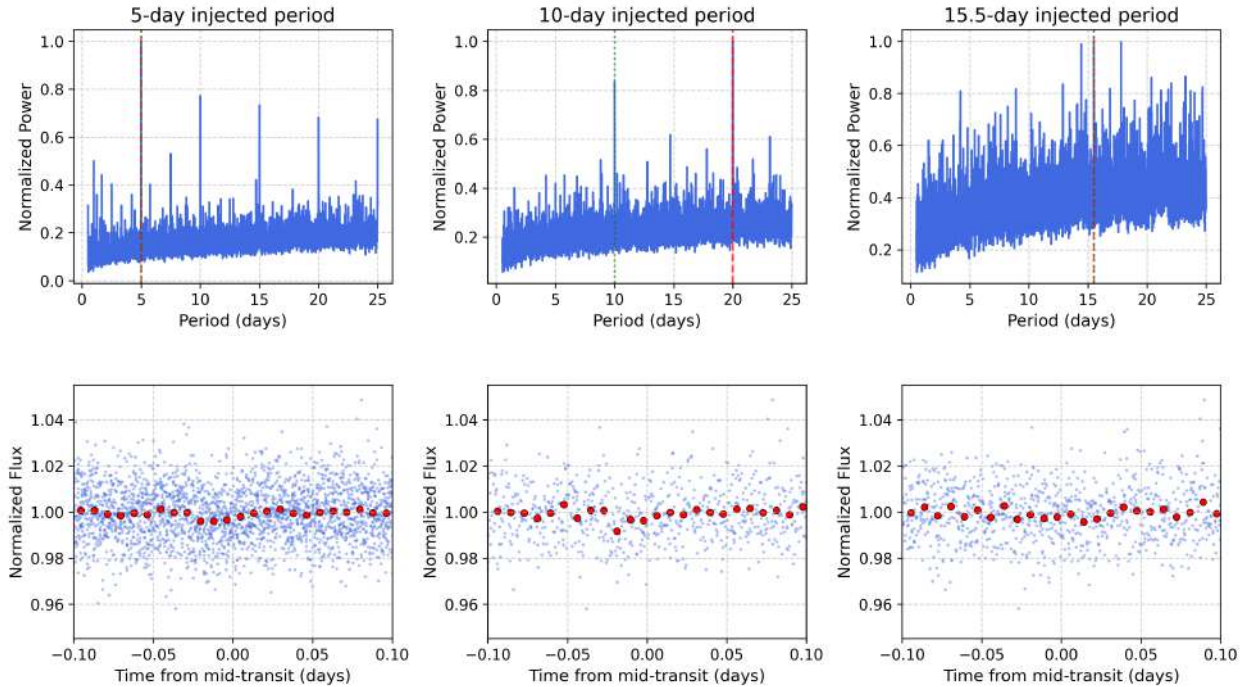


Figure 5: Top row: BLS periodograms for each injected orbital period (green dotted line), with detected periods marked by red dashed lines. Bottom row: Phase-folded light curves centered on the detected signals, showing both original data (blue) and 12-minutes-binned points (red).

For the 5-day injection, the BLS algorithm correctly recovers the injected period, yielding a Signal Detection Efficiency (SDE) of 15.42, well above the adopted significance threshold of SDE = 7. This indicates a strong and unambiguous detection. The periodogram also displays alias peaks at integer multiples of the true period (10, 15, 20, and 25 days). This structure is typical for short-period transits and offers a useful comparison to the real TESS periodogram in Figure 4, where such signatures are not present, suggesting that no comparable short-period transit signals exist in the original data. In the case of the 10-day injection, the BLS identifies the 20-day harmonic (i.e., the first alias) as the strongest peak rather than the true period. The corresponding SDE of 12.46 still indicates a statistically significant detection. This aliasing is a well-known effect, particularly in datasets with irregular sampling or when only a limited number of transits are sampled. For the 15.5-day injection, the BLS does recover the correct period. However, the resulting SDE is 5.9, falling just below the detection threshold. The corresponding periodogram lacks a distinct peak, reflecting the reduced detection significance. This is likely due to the limited number of transits present within the TESS observing window. Residual variability near transit phases (see third panel in Figure 5) likely also obscures these shallow transits, further reducing detection significance.

These outcomes illustrate two key limitations of transit detection in the TESS light curves:

- **Alias Ambiguity:** Periodogram peaks at harmonics of the true period can lead to incorrect detections when transit coverage is sparse.
- **Reduced Sensitivity at Long Periods:** As the orbital period increases, fewer transits occur in the data, lowering the detection significance and making it harder to distinguish the transit signal from noise.

Additionally, the use of idealized, box-shaped transits likely overestimates the detectability of real planets. In practice, limb darkening causes transit shapes to deviate from this form, further reducing detection sensitivity.

To assess the detectability of the candidate planet with TESS more systematically, we performed an injection-recovery test using the `Nuance` package (Garcia et al., 2024). Synthetic transit signals were injected into the observed data, and their recovery was evaluated. We explored planetary radii from $0.05 R_{\oplus}$ to $2.5 R_{\oplus}$. The signal-to-noise ratio (SNR) for each scenario was computed and a threshold of SNR = 6 was adopted, balancing sensitivity with false positive suppression. Figure 6 presents the recovery efficiency for different planetary radii and periods.

As can be seen in Figure 6, the candidate planet is near the threshold of detectability in TESS data, with its recovery probability strongly dependent on its true radius and period. The primary source of uncertainty in its size arises from the uncertainty in the stellar radius of SP1036+1923 (see Table 1). A planet of $1.002 R_{\oplus}$ has an 80 % recovery for a 5-day period, dropping to 60% for 10 days and only 10% for 15.5 days. If the planet is on the larger end of the estimated radius range, it should be detected in TESS data (100% recovery at 5 and 10 days, 70% at 15.5 days). Conversely, if it is on the smaller end, its detectability significantly decreases (70% at 5 days, 10% at 10 days and 0% at 15.5 days). The absence of a detection in TESS suggests one of three possibilities: (1) the planet’s true radius is at the lower end of its uncertainty range, reducing its signal below the detection threshold, (2) the orbital period is longer than 10 days, making it harder to detect in the available TESS data, or (3) the observed dip in Figure 1 is a false positive or caused by, for example, stellar variability. Therefore, TESS data alone is insufficient to confirm or rule out the candidate.

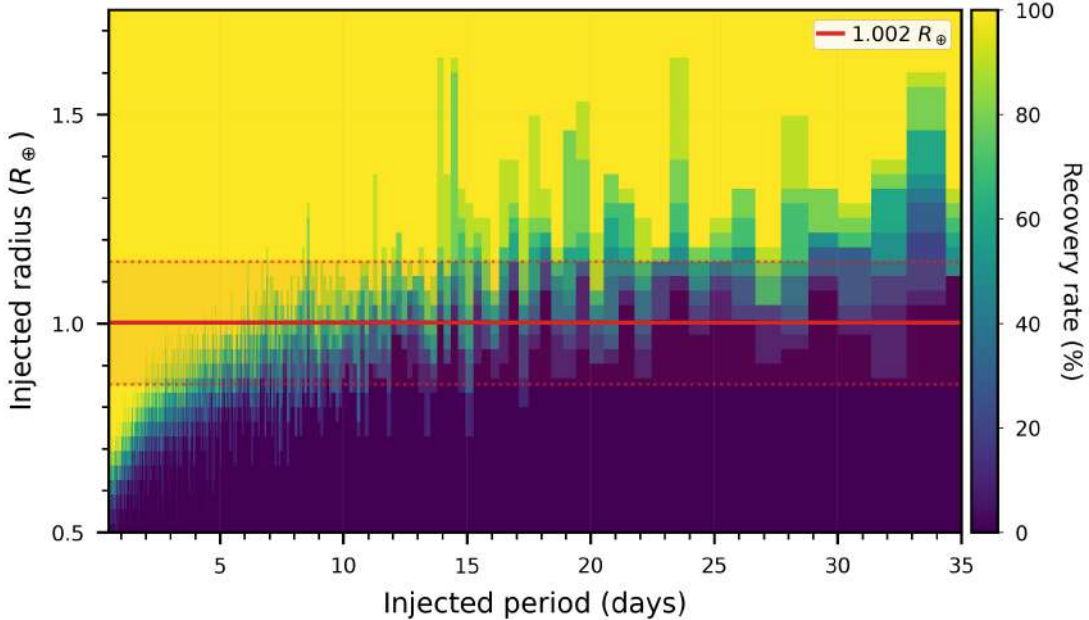


Figure 6: Transit recovery efficiency. The color scale represents the fraction of recovered signals with $\text{SNR} > 6$. The red line indicates the candidates estimated size ($1.002 R_{\oplus}$), with the shaded region indicating uncertainty.

3.3 MCMC Fit of the Transit Candidate

To further investigate this potential transit, we now turn to another approach: MCMC fitting of a transit model to the SAINT-EX single-transit event. This method allows us to explore plausible orbital parameters and assess the likelihood of a planetary origin.

The potential transit was modeled using the `batman` package (Kreidberg, 2015), which implements the analytical transit model of (Mandel & Agol, 2002), as described in Section 1.1.1.

Quadratic limb-darkening coefficients were determined using the `LDTk` Python package (Parviainen & Aigrain, 2015), which calculates these coefficients based on the PHOENIX stellar atmosphere models (Husser et al., 2013). The input stellar parameters effective temperature T_{eff} and surface gravity $\log g$ were taken from (Wang et al., 2022). Metallicity ([Fe/H]) is not available for this target, so a typical value for M6.5 stars was adopted with a broad uncertainty to reflect the lack of precise constraints. The stellar mass of the target is reported to be $0.111 \pm 0.001 M_{\odot}$, and the radius $R_{\star} = 0.137 \pm 0.020 R_{\odot}$ (Sebastian et al., 2021). The stellar density was derived from mass and radius via

$$\rho_{\star} = \frac{3M_{\star}}{4\pi R_{\star}^3}, \quad (17)$$

with propagated uncertainties yielding a 15% error. Additionally, we accounted for a potential deviation from the expected out-of-transit flux level of 1 by fitting for the baseline flux F_0 . On this we put a Gaussian prior centered on the median out-of-transit flux, with a width equal to the flux RMS. The posterior distributions of the transit parameters were sampled using the affine-invariant MCMC ensemble sampler `emcee` (Foreman-Mackey et al., 2013). A total of 64 walkers were initialized on the parameter estimates and ran the chains for 20,000 steps, discarding the first 8,000 steps as burn-in and thinning the remaining chain by a factor of 10 to reduce autocorrelation. The adopted priors are summarized in Table 3.

Table 3: Prior Distributions for Transit Parameters of SP1036+1923

Parameter	Prior	Units
Mid-transit time (t_0)	$\mathcal{N}(2460383.7425, 0.025)$	BJD _{TDB}
Orbital period (P)	$\mathcal{U}(0.1,)$	days
Radius ratio (R_p/R_\star)	$\mathcal{U}(0.0, 1.0)$	–
Impact parameter (b)	$\mathcal{U}(0.0, 1.0)$	–
Limb-darkening coefficient (u_1)	$\mathcal{N}(0.347, 0.15)$	–
Limb-darkening coefficient (u_2)	$\mathcal{N}(1, 0.005)$	–
Baseline Flux (F_0)	$\mathcal{N}(0.358, 0.15)$	–
Stellar density (ρ_\star)	$\mathcal{N}(60911.64, 9136.75)$	kg m^{-3}
Eccentricity (e)	Fixed at 0	–
Transit duration (T_{dur})	$\mathcal{U}(0.02, 0.05)$	days

The best-fit transit model is shown in Figure 7, and the corresponding corner plot is displayed in Figure 8.

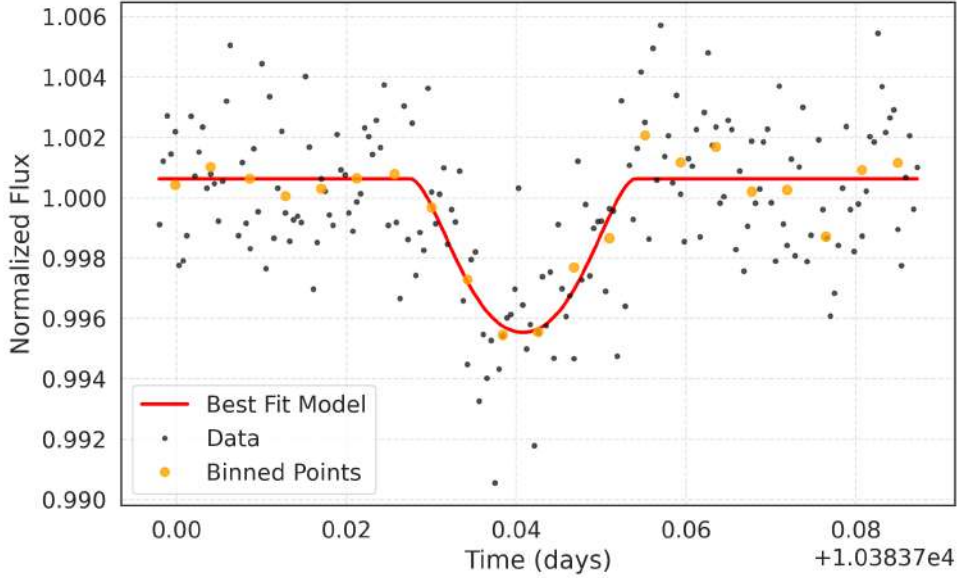


Figure 7: Best-fit transit model (red line) to the SAINT-EX photometry (black points). Orange circles show 9-point binned data for visualization.

The best-fit model shows good convergence with the observed data, exhibiting no significant systematic trend in the residuals. The resulting parameters from the model fit are listed in Table 4.

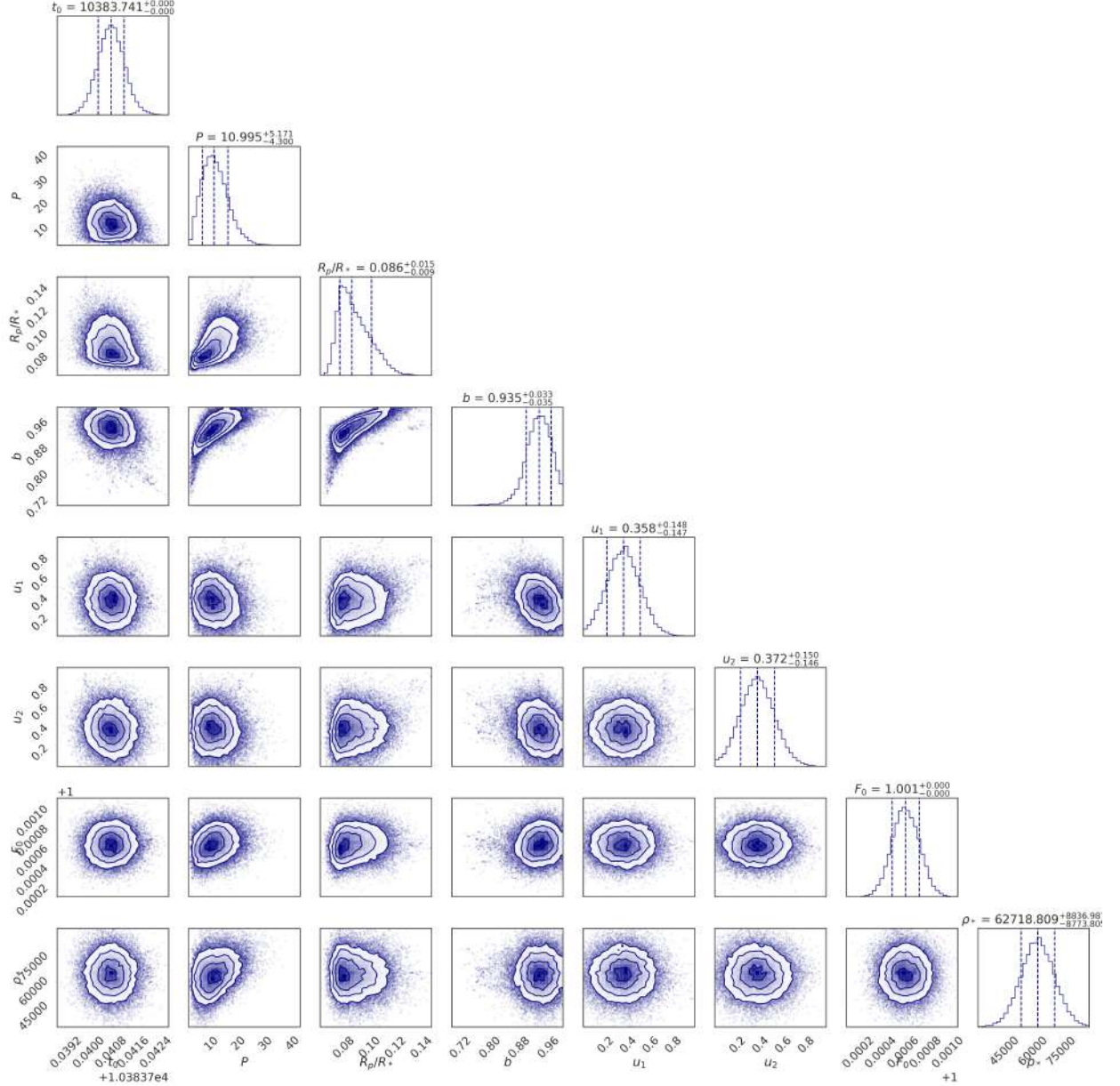


Figure 8: Corner plot showing the posterior distributions of the fitted parameters from the MCMC analysis of SP1036+1923. The solid lines in the 1D histograms represent the median values, and the dashed lines indicate the 16th and 84th percentiles (1 σ credible intervals).

Table 4: Results of the MCMC fit for SP1036+1923.

Parameter	Result
Mid-transit time (t_0)	$2460383.741^{+0.00013}_{-0.00011}$ (BJD _{TDB})
Orbital period (P)	$10.995^{+5.171}_{-4.300}$ (days)
Radius ratio (R_p/R_\star)	$0.086^{+0.015}_{-0.009}$
Impact parameter (b)	$0.935^{+0.033}_{-0.035}$
Limb-darkening coefficient (u_1)	$0.358^{+0.148}_{-0.147}$
Limb-darkening coefficient (u_2)	$0.372^{+0.150}_{-0.146}$
Baseline Flux (F_0)	$1.001^{+0.0002}_{-0.0002}$
Stellar density (ρ_\star)	$62718.809^{+8836.987}_{-8773.805}$ (kg m ⁻³)
Transit duration (T_{dur})	$0.0266^{+0.00228}_{-0.00270}$ (days)

Given R_p/R_\star the radius of the planet would be 1.285 ± 0.292 Earth radii. Based on these posteriors scaled semi-major axis and orbital inclination were computed. This yields $\frac{a}{R_\star} = 73.73 \pm 21.45$ and $i = 89.27^\circ \pm 0.21^\circ$. The large uncertainty in $\frac{a}{R_\star}$ is consistent with the broad posterior on the orbital period. Convergence of the parameters was evaluated using the \hat{R} statistic introduced by [Gelman & Rubin \(1992\)](#). The parameters u_1 , u_2 , F_0 and ρ_\star all met $\hat{R} < 1.01$, while the less constrained parameters P , R_p/R_\star and b fulfilled $\hat{R} < 1.02$ which is a widely used and accepted threshold ([Vats & Knudson, 2018](#)).

We note that the spread in ρ_\star , u_1 and u_2 largely reflect the width of their Gaussian priors. This suggests that the data did not significantly constrain these parameters. This is understandable, given the limited data quality from a single transit event. Still, it's worth emphasizing that the priors themselves are physically grounded. Despite this, the less informed parameters P , R_p/R_\star and b were able to converge and remain meaningfully constrained. This supports the robustness of the chosen parameterization and prior setup. In addition to the presented parametrization, alternatives were tested, including simpler setups, given the limited data quality. However, the chosen parameterization strikes a balance between avoiding unnecessary complexity and effectively incorporating prior knowledge, while allowing for meaningful inference.

In the corner plot (Figure 8), we can see a degeneracy between the impact parameter (b) and the orbital period (P), a known challenge for single-transit events ([Osborn et al., 2016](#)). This degeneracy arises because the impact parameter influences the observed transit duration (T_{dur}), which is also dependent on the orbital period. Specifically, for a circular orbit, the transit duration scales as in equation (5). This creates a family of (b, P) solutions that produce nearly identical transit shapes and durations when only one event is observed. There is also a degeneracy between b and R_p/R_\star , here the relationship is more complex. For higher b , the transit becomes shallower and shorter (because the planet crosses the dimmer edges of the stellar disk). To reproduce the same observed transit depth, a larger planet-to-star radius ratio is required. However, this compensation is not straightforward, as the precise effect also depends on the specific limb darkening profile.

The posterior distribution of the orbital period is shown in Figure 9. Our analysis constrains the period to $11.0^{+5.2}_{-4.3}$ days (median and 68% credible interval). The injection-recovery tests (Figure 6) exclude periods < 5 days, as these would have been detected in TESS data. Together with the limit from the MCMC model approach, the period still remains rather broad for targeted follow-up observations.

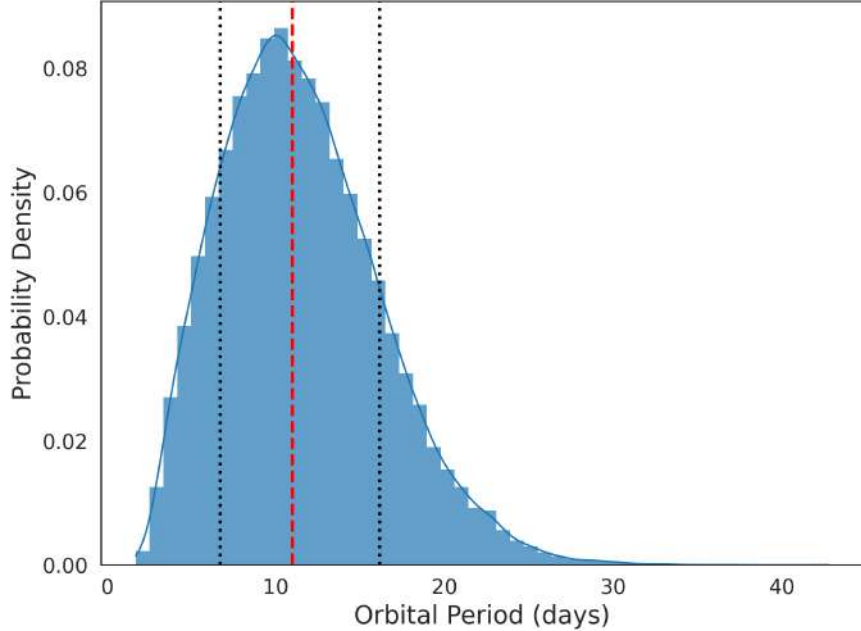


Figure 9: Posterior distribution of the orbital period derived from MCMC sampling. The blue histogram represents the probability density of the period. The red dashed line indicates the median period ($P = 11.0$ days), while the black dotted lines mark the 16th (6.67 days) and 84th (16.17 days) percentiles, representing the credible interval. The Kernel Density Estimate (KDE) is overlaid to provide a smooth representation of the distribution.

3.4 Inspection of SPECULOOS Data

As a next step, all available data for this target from the SPECULOOS project were compiled. Several light curves exhibit variability. Possible causes for this photometric variability in a mid-M dwarf include stellar activity such as star spots or the presence of an unresolved eclipsing binary companion (Newton et al., 2016). Some of the observed features visually resemble transit-like signals, as they also manifest as dips in the flux. However, the timescales of these features vary, which raises the possibility that the initial transit-like event might also originate from stellar variability rather than a genuine planetary transit. On the other hand, it is also plausible that some of these variability pattern may include actual transits embedded within broader flux modulations. To explore this possibility, we constructed a trial period grid ranging from 7 to 25 days, informed by the constrained period distribution of the initial transit candidate. This grid was used to test whether any of the observed flux dips align with the initial candidate plausible periods that are not excluded by the other available data. This search yielded a candidate period of 13.148 days. For this period, two events were found to coincide with the predicted transit times, as highlighted by the vertical dashed red lines in Figure 10. The data was also phase-folded using the candidate period of 13.148 days. The resulting light curve is shown in Figure 11. A clear dip is visible around the predicted transit center, supporting the plausibility of this period and motivating further analysis.

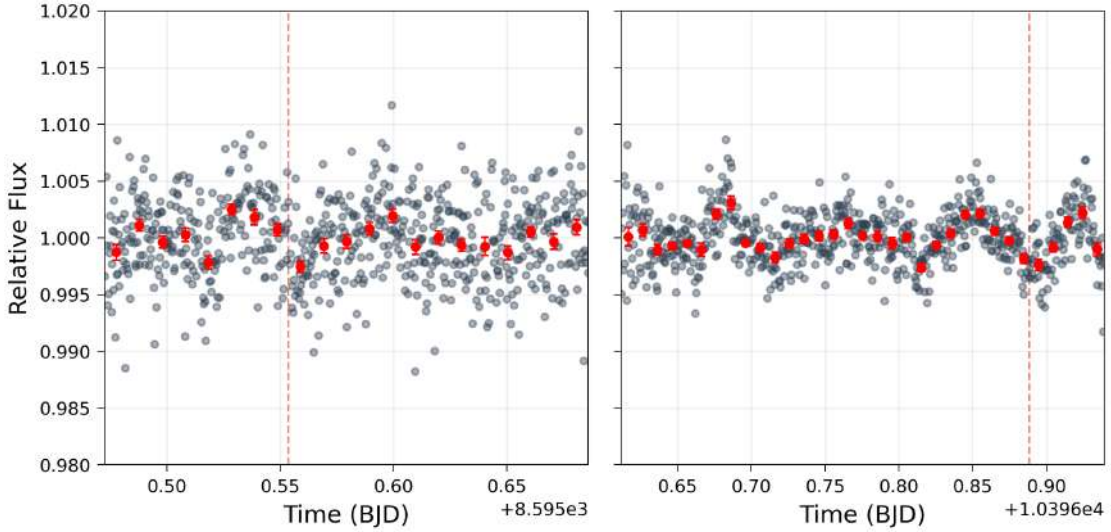


Figure 10: Candidate transit-like signals in SPECULOOS light curves of SP1036+1923. Each panel shows one observing night with predicted transit times (dashed red lines). Over-plotted are binned flux points (red circles) with 14-minute bins.

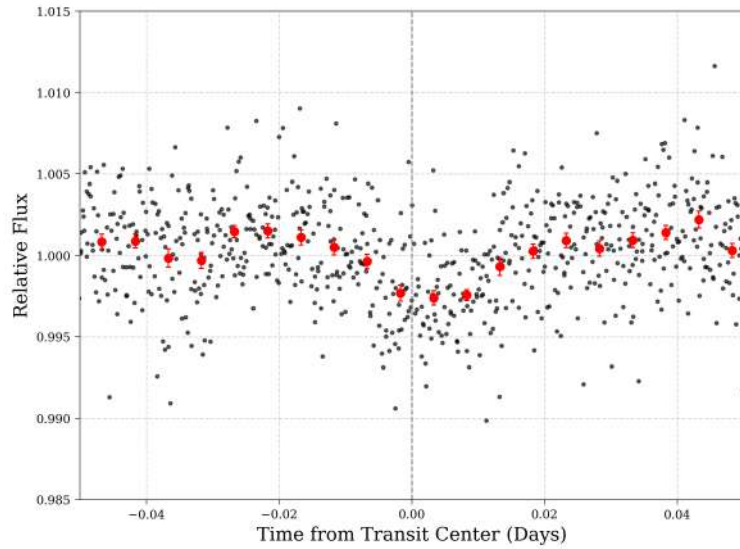


Figure 11: Folded light curve using a trial period of 21.30 days. Individual flux measurements are shown in black, with red points indicating binned flux values and associated uncertainties. The vertical dashed line marks the expected transit center.

3.5 Discussion

The MCMC fit successfully constrained the parameters of the potential planet-star system. The derived planetary radius is 1.285 ± 0.292 Earth radii, and thus larger than initially estimated through visual inspection of the light curve pattern. Revisiting the TESS injection-recovery experiment (Figure 6), this suggests that, given this refined radius, the detection of such a planet should be more likely. However, the planet radius still carries a large uncertainty and remains near the threshold of detectability, especially considering the lower bound of the radius estimate and the upper end of the plausible period range. It is also possible that the detrending applied to the initial transit pattern introduced a slight bias, potentially deepening the apparent transit and thus leading to an overestimated planetary radius.

The variability patterns observed in the SPECULOOS data raise the possibility that the initial transit-like signal is a result of the same underlying variability, which may not be of planetary origin. However, the candidate period of 13.148 days, along with the phase-folded light curve (Figure 11), suggests a good alignment. This recurrence and alignment of flux dips across different nights is noteworthy. This motivates further investigation of the system and the data. One possible next step could be an MCMC fit to the phase-folded light curve.

Given these findings, follow-up observations, particularly for the candidate period of 13.148 days seems worthwhile. These could either confirm periodicity or further characterize the nature of the variability. More broadly, the system would benefit from refined stellar characterization to narrow down estimates. Radial velocity measurements could provide independent confirmation of a planetary companion, and continued photometric monitoring may enable the detection of subsequent events.

4 SP0314+1603: Light Curve Analysis

SP0314+1603 is part of the SPECULOOS target list (Sebastian et al., 2021). It is classified as a peculiar M9 dwarf with an estimated age of 500 Myr at a distance of 13.6 pc (Gagné et al., 2015). Given its parameters reported in Table 5, it is a compelling target at the edge between low-mass star and brown dwarf.

Table 5: Fundamental parameters of the target star SP0314+1603.

Parameter	Value
ICRS Coordinates (J2000)	03:14:03.4425 +16:03:05.4723
Spectral Type	M9
Photometric Fluxes	
<i>G</i> -band magnitude	17.2
<i>J</i> -band magnitude	12.5
<i>K</i> -band magnitude	11.2
Stellar Radius	
Stellar Radius	$0.107 \pm 0.002 R_{\odot}$
Stellar Mass	
Stellar Mass	$0.068 \pm 0.003 M_{\odot}$
Effective Temperature (T_{eff})	
Effective Temperature (T_{eff})	2250 K
Surface Gravity ($\log g$)	
Surface Gravity ($\log g$)	5.5

4.1 Initial Transit Candidate

The light curve of Sp0314+1603, observed on 24 September 2022 with the SPECULOOS/Europa telescope using the I+z filter and 70-second exposures, exhibits a transit-like feature (Figure 12). To assess the robustness of this signal, a series of validation steps were performed. The photometric data was detrended using a weighted linear regression model that accounted for instrumental and atmospheric systematics. Specifically, the model included the squared full width at half maximum (FWHM²), squared sky background (SKY²), squared positional shifts in right ascension and declination (dRA^2 and $dDEC^2$), and squared airmass (AIRMASS²). The regression was performed using weighted least squares. The resulting trend was then subtracted from the original flux. The data was also flattened using a rolling median filter. The resulting light curve showed significantly improved photometric precision, with the RMS scatter reduced from 8.14 ppt to 5.5 ppt. Importantly, the distinct transit-like feature remained clearly visible at BJD 2459847.87, indicating that it is unlikely to be caused by systematics (see light curve in the right panel of Figure 12).

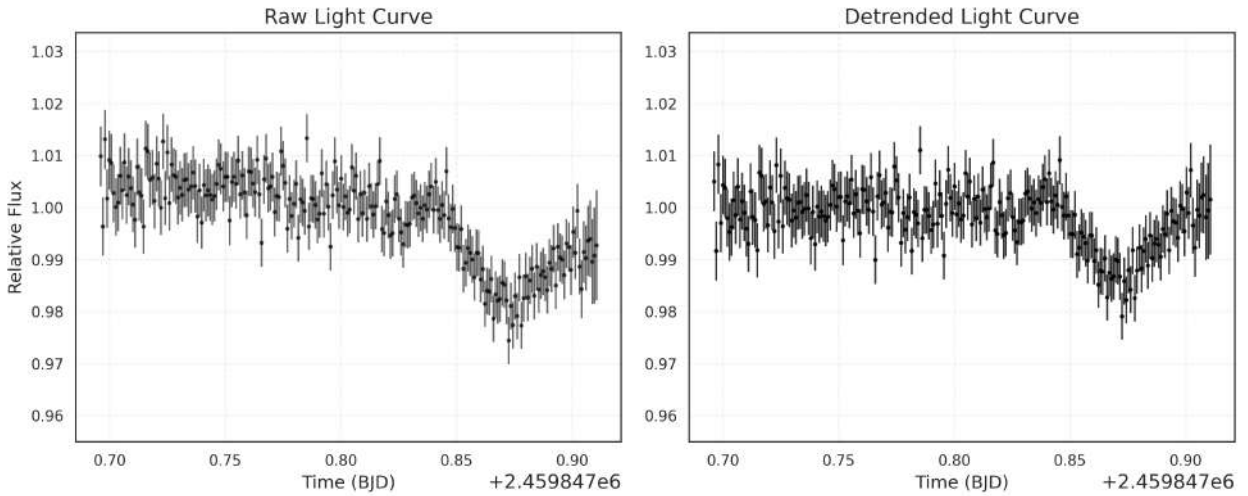


Figure 12: Light Curve of the target SP0314+1603 from the night of 2022-09-24. **Left:** Original light curve. **Right:** Detrended light curve. Black points show individual measurements with the spline-detrended result.

4.2 TESS Photometry

As with the previous target (see Section 3.2), we analyzed the available TESS data for SP0314+1603. The target was observed in Sector 43 and 44 with both 120-second and 600-second cadence modes. The light curves were processed following the same procedure, removing NaNs and outliers, then flattening using an optimized window length. Figure 13 shows the 120s exposure dataset before and after detrending.

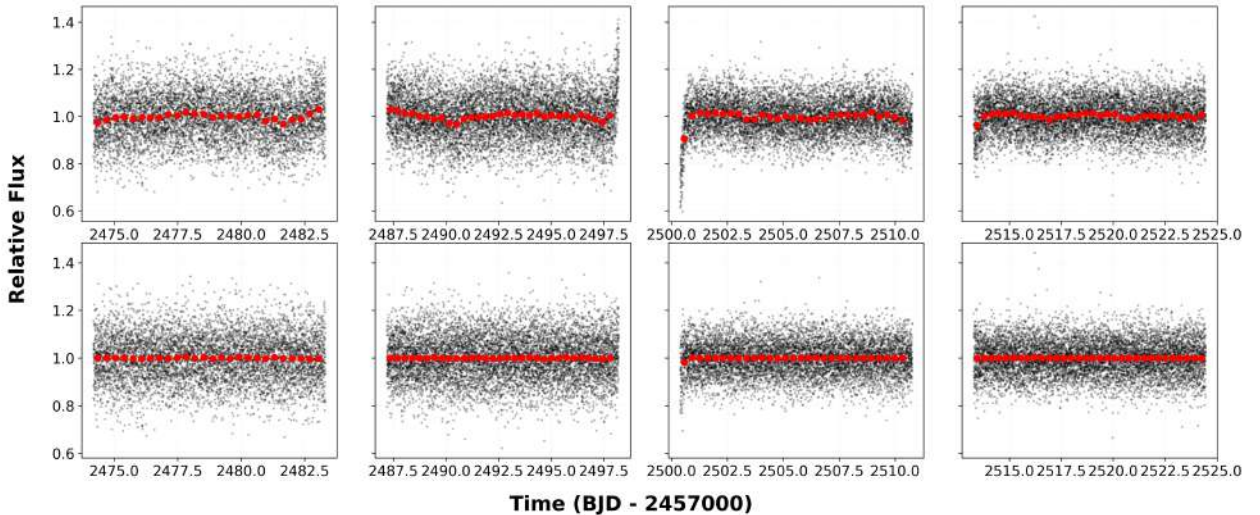


Figure 13: TESS light curve for SP0314+1603 before (top) and after (bottom) detrending. The raw flux (top) and detrended flux (bottom) are shown with individual data points (black) and binned points (red).

The resulting BLS periodogram is shown in Figure 14. The peak in BLS power occurs at a period of 11.794 days, a transit epoch (t_0) of 2476.1140 (BJD) with a corresponding transit duration of 1.20 hours and a depth of 27.28 ppt. However, both the transit morphology and ephemeris are inconsistent with the potential transit event observed by EUROPA. Additionally, the calculated Signal Detection Efficiency (SDE) of 5.85 falls below the significance threshold, indicating a likely false positive.

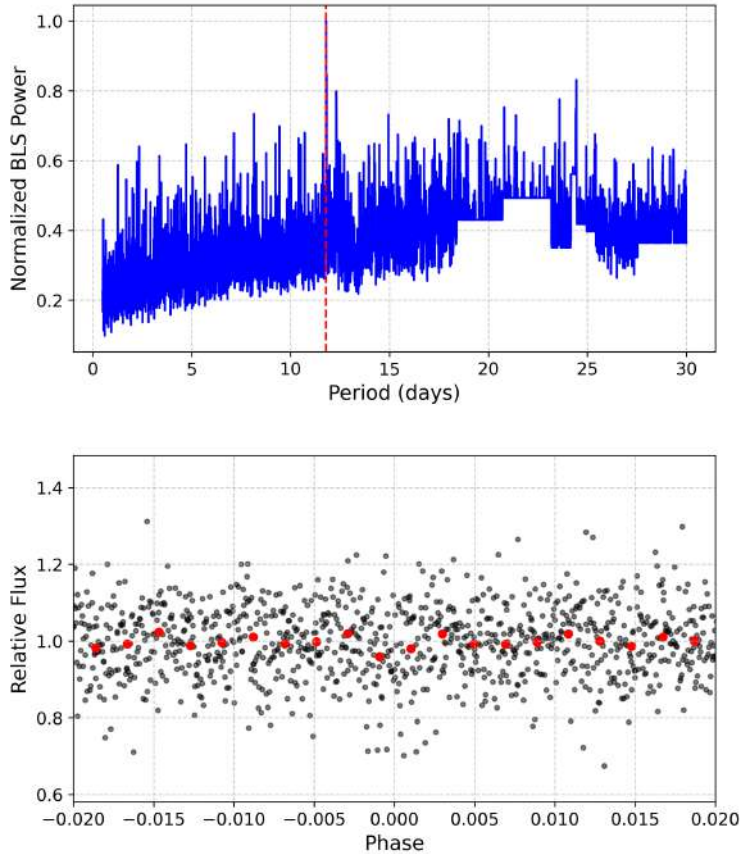


Figure 14: Analysis of TESS 120s cadence data. **Top:** BLS periodogram showing peak power at 11.794 days (red dashed line). **Bottom:** Phase-folded light curve centered on the candidate transit, with binned points in red and unbinned in black.

The periodogram shows an unusual pattern starting around 18 days (sharp, cut-off bottom). This is likely due to the observational window function, as data gaps are known to introduce artificial structures in periodograms (Hippke & Heller, 2019).

4.2.1 Injection-Recovery Analysis

To assess the sensitivity of TESS for this system, we conducted an injection-recovery analysis following the approach described in Section 3.2.1. Synthetic transits were injected over a grid of orbital periods and planetary radii, and their detectability was evaluated with an SNR threshold of 6.

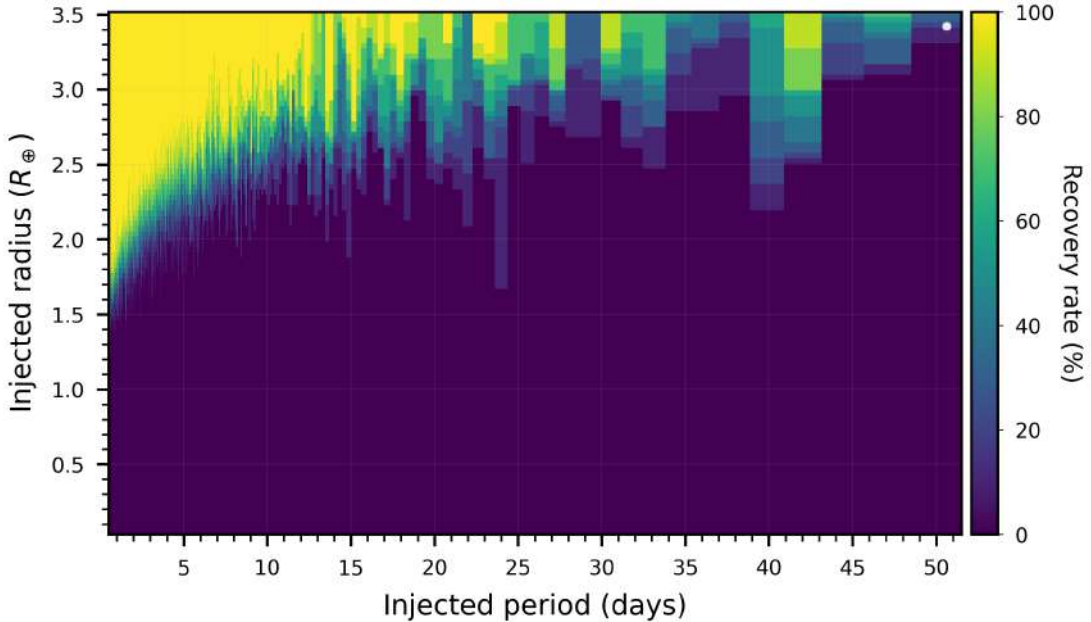


Figure 15: Transit recovery efficiency for SP0314+1603. Color scale indicates the fraction of successfully recovered signals with $\text{SNR} > 6$.

As shown in Figure 15, TESS is not sensitive to shallow transits in this system. For SP0314+1603, the reported stellar radius is $0.107 R_\odot$, so a transit depth of 10 ppt would correspond to a planetary radius of $R_p \approx 1.17 R_\oplus$. This falls well below the recovery threshold across the entire period range. In fact, planets smaller than $1.5 R_\oplus$ are not detectable in this system. This illustrates that TESS is not feasible for detecting the planetary candidate in question, and it motivates ground-based follow-up and alternative detection strategies.

4.3 MCMC Fit of the Transit Candidate

Following the same procedure as in Section 3.3, we pursued an MCMC fit to the initial transit-like pattern. Stellar limb-darkening coefficients were computed using the LDTK package (Parviainen & Aigrain, 2015), based on T_{eff} and $\log g$ from Gagné et al. (2015), assuming stellar metallicity with conservative uncertainties. The stellar density was derived with propagated uncertainties yielding a 7.5% error. This error is smaller than for SP1036+1923, due to better-constrained stellar parameters. A total of 64 walkers were initialized at preliminary parameter estimates and ran the chains for 20,000 steps, discarding the first 8,000 steps as burn-in and thinning the remaining chain by a factor of 10 to reduce autocorrelation. The adopted priors are summarized in Table 6.

Table 6: Prior Distributions for Transit Parameters, SP0314+1603

Parameter	Prior	Units
Mid-transit time (t_0)	$\mathcal{N}(2459847.88, 0.025)$	BJD _{TDB}
Orbital period (P)	$\mathcal{U}(0.1,)$	days
Radius ratio (R_p/R_\star)	$\mathcal{U}(0.0, 1.0)$	—
Impact parameter (b)	$\mathcal{U}(0.0, 1.0)$	—
Limb-darkening coefficient (u_1)	$\mathcal{N}(0.530, 0.15)$	—
Limb-darkening coefficient (u_2)	$\mathcal{N}(0.249, 0.15)$	—
Baseline Flux (F_0)	$\mathcal{N}(1, 0.005)$	—
Stellar density (ρ_\star)	$\mathcal{N}(79274.49, 6091.5)$	kg m^{-3}
Eccentricity (e)	Fixed at 0	—
Derived Parameters		
Scaled semi-major axis (a/R_\star)	—	—
Inclination (i)	—	deg
Transit duration (T_{dur})	$\mathcal{U}(0.041, 0.055)$	days

Figures 16 and 17 show the best-fit transit model and posterior distributions. The model adequately fits the light curve, with no systematic trends in the residuals. Convergence of the parameters was ensured using the \hat{R} statistic introduced by [Gelman & Rubin \(1992\)](#). The resulting parameters from the model fit are listed in Table 7.

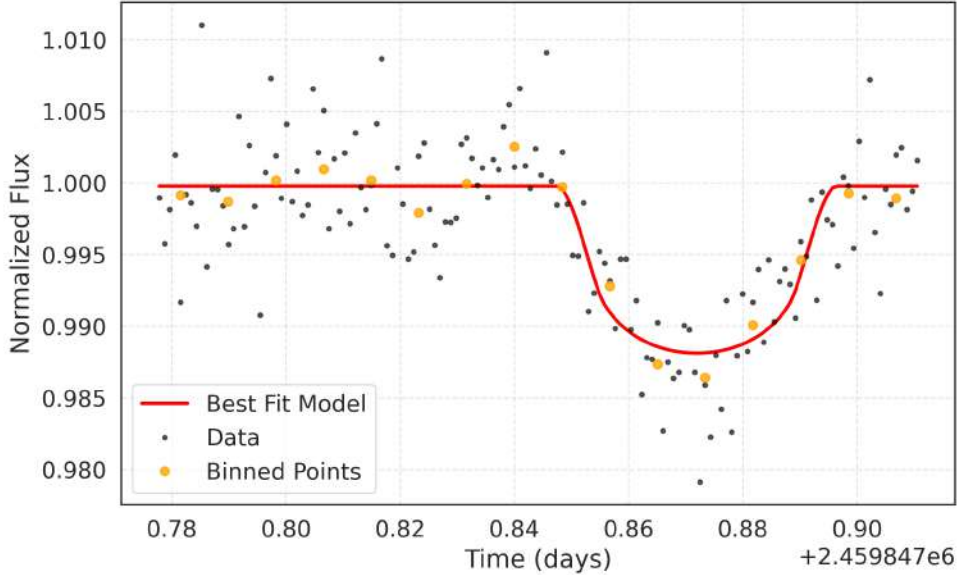


Figure 16: Transit light curve fit to the observed data. The black points represent the individual flux measurements, while the orange circles show the binned data (9-point bins) for clarity. The red line represents the best-fit transit model derived from the MCMC analysis.

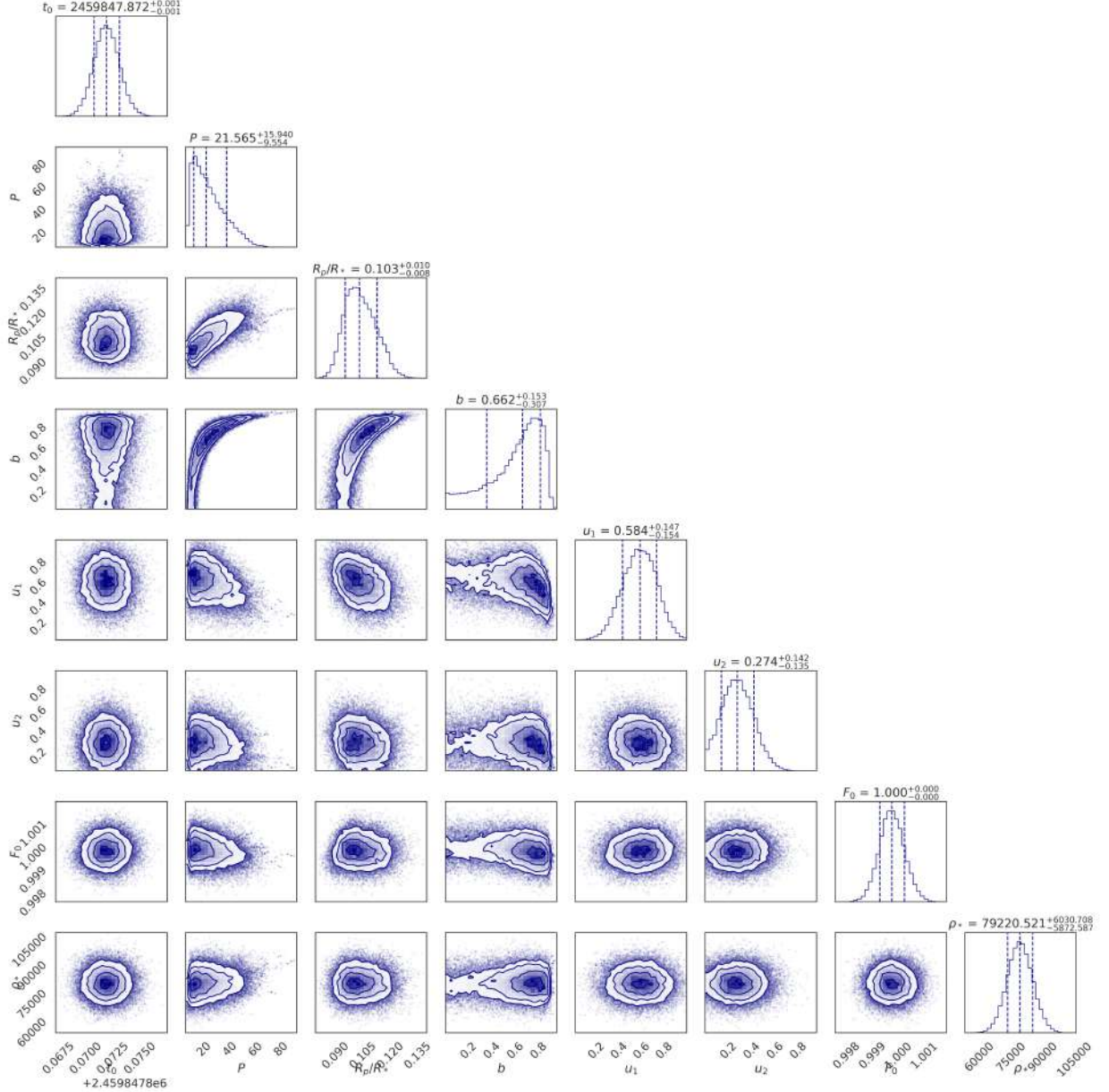


Figure 17: Corner plot showing the posterior distributions of the fitted parameters from the MCMC analysis for SP0314. The solid lines in the 1D histograms represent the median values, and the dashed lines indicate the 16th and 84th percentiles (1σ credible intervals).

Table 7: Results of the MCMC fit for SP0314+1603.

Parameter	Result
Mid-transit time (t_0)	$2459847.872^{+0.001}_{-0.001}$ (BJD _{TDB})
Orbital period (P)	$21.565^{+15.940}_{-9.554}$ (days)
Radius ratio (R_p/R_\star)	$0.103^{+0.010}_{-0.008}$
Impact parameter (b)	$0.662^{+0.153}_{-0.307}$
Limb-darkening coefficient (u_1)	$0.584^{+0.147}_{-0.154}$
Limb-darkening coefficient (u_2)	$0.274^{+0.142}_{-0.135}$
Baseline Flux (F_0)	$1.000^{+0.0002}_{-0.0002}$
Stellar density (ρ_\star)	$79220.521^{+6030.708}_{-5872.587}$ (kg m ⁻³)
Transit duration (T_{dur})	$0.04870^{+0.0029}_{-0.0036}$ (days)

Given R_p/R_\star the radius of the planet would be 1.202 ± 0.119 Earth radii. The scaled semi-major axis is calculated to be $\frac{a}{R_\star} = 144.96 \pm 43.24$ and the inclination $i = 89.72^\circ \pm 0.09^\circ$. These parameters bear some resemblance to those of TRAPPIST-1.h, the outermost known planet in the TRAPPIST-1 system, which has a median orbital period of approximately 20 days and a scaled semi-major axis around $a/R_\star \approx 117$, also with relatively large associated uncertainties (Gillon et al., 2017).

Similar to the MCMC fit of SP1036+1923, the posterior spreads in ρ_\star , u_1 and u_2 largely reflect the width of their priors. The same considerations discussed in Section 3.3 apply here, noting that the priors are physically grounded.

The posterior distribution of the orbital period (Figure 18) spans a broad range, with a median of 21.565 days and a 1σ interval of 12.01 to 37.50 days. This wide range underscores the inherent uncertainty in single-transit modeling, where the data offer limited constraints on periodicity. However, the analysis was able to place a meaningful lower bound on the period, effectively ruling out orbital periods shorter than 5 days.

The SPECULOOS observations of SP0314+1603 span a total of 306.77 hours and reveal significant photometric variability. Several features within the light curve resemble possibly transit-like events. An initial attempt was made to detrend and model a subset of these signals using the same MCMC framework. However, this untargeted and time-intensive approach did not yield meaningful insights. Many of these features likely stem from stellar variability. The lack of a clear second transit event and the presence of significant variability make it difficult to confidently identify any of these features as planetary in origin. Given these challenges, we adopt a more holistic approach, using the full SPECULOOS dataset.

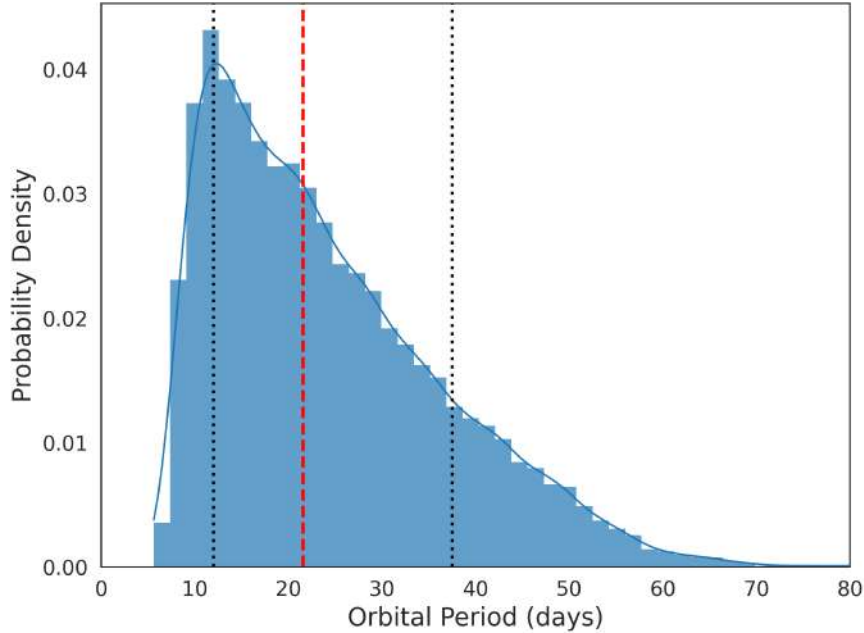


Figure 18: Posterior distribution of the orbital period derived from MCMC sampling. The blue histogram represents the probability density of the period, normalized such that the total area under the curve sums to 1. The red dashed line indicates the median period ($P = 21.565$ days), while the black dotted lines mark the 16th (12.01 days) and 84th (37.50 days) percentiles, representing the credible interval. The Kernel Density Estimate (KDE) is overlaid to provide a smooth representation of the distribution.

4.4 Modeling of Stellar Variability

The target, SP0314+1603, is an active M9 dwarf and possibly a brown dwarf. As described in Section 1.4 these objects are known for significant photometric variability. These dynamic processes impede the search for periodic transit signals in the light curves of such objects, especially when the timescale and amplitude of stellar fluctuations are similar to those of a potential planetary transit. The challenge therefore lies in modeling the stellar variability while preserving any underlying planetary signals.

4.4.1 Data Reduction

When addressing long-term stellar variability, particularly signals spanning multiple nights, care must be taken with detrending methods such as high-pass filtering, polynomial fitting, or aggressive flattening. These techniques can remove astrophysical signals of interest. Therefore, for the variability analysis presented in this section, we apply only minimal initial preprocessing to the photometric data. This includes flux normalization and the removal of NaNs and statistical outliers. This conservative approach helps preserve intrinsic stellar variability, ensuring that key astrophysical signals are not artificially suppressed.

In parallel, the dataset was also detrended using an approach similar to the one described in Section 4.1. This more advanced reduction yielded a 15.7% improvement in RMS scatter.

For the following analysis, we use the lightly processed dataset, as it better preserves the low-frequency stellar variability. Nevertheless, all results were also cross-checked using the more strongly detrended version to validate the findings.

4.4.2 Initial Steps and Diagnostics

As an initial step in the search for transits in the *SPECULOOS* light curves of SP0314+1603, we applied a Box Least Squares (BLS) periodogram. The peak in the periodogram corresponded to a period of 3.81 days with a depth of 1.3%. However, detailed examination revealed this signal did not match expected transit morphology and no significant SDE. We therefore attribute this signal to stellar variability or systematics rather than a genuine planetary transit.

To independently probe periodic behavior in the light curve, we computed the autocorrelation function (ACF). This technique is sensitive to quasi-periodic variability and offers a diagnostic by identifying correlations in flux at various time lags. In figure 19 the ACF of the data of SP0314+1603 is displayed.

The ACF displays a peak at a lag of 1.35 days (excluding lags < 0.1 days). It exceeds the 95% confidence interval, indicating that the autocorrelation at this lag is unlikely due to random white noise. However, the confidence interval should be interpreted with caution, as it is well known that time-correlated ("red") noise can bias significance estimates, particularly in data with strong photometric variability (Pont et al., 2006). The multiples of the maximum ACF value do align with some local peaks, they are however not significant and seem to wash out over longer timescales, suggesting a more complex signal structure. Furthermore, the ACF values weaken for longer time lags, indicating that the periodicity is not stable over extended periods. This behavior could be attributed to several factors, such as the accumulation of random noise, a finite correlation length, long-term trends that weaken the autocorrelation at longer lags, or the uneven sampling of the data. Additionally, fewer data pairs are available at longer lags, which increases statistical uncertainty and may contribute to the decrease in ACF strength. The strong and rapid decay at the beginning of the ACF suggests that the light curve varies significantly over short timescales. The autocorrelation analysis confirms the presence of correlated variability, likely tied to the star's rotation and atmospheric dynamics. Given the quasi-periodic structure, it also highlights the complexity and non-stationarity of the signal, complicating periodic transit searches.

To further investigate periodicity, we applied a Lomb-Scargle periodogram to the same light curve (Figure 20).

The Lomb-Scargle analysis identifies a dominant periodicity at 0.64 days, which exhibits an approximate 2:1 ratio with the ACF peak ($1.35/0.64 \approx 2.1$). The 0.64-day signal could represent the first harmonic of a true 1.35-day period pattern, or vice versa. Alternatively, both signals might be harmonics of a more fundamental shorter period (e.g., 0.33 days), consistent with findings that late-type M dwarfs often exhibit rotation periods shorter than one day (Newton et al., 2016). The slight deviation from an exact 2:1 ratio may arise from noise, irregular sampling, or evolution in the signal over time. Additionally, if the variability is not strictly sinusoidal, different period-finding methods can yield different dominant periodicities (VanderPlas, 2018). Additional long-baseline photometric monitoring or radial velocity follow-up is required to resolve the true nature of the variability.

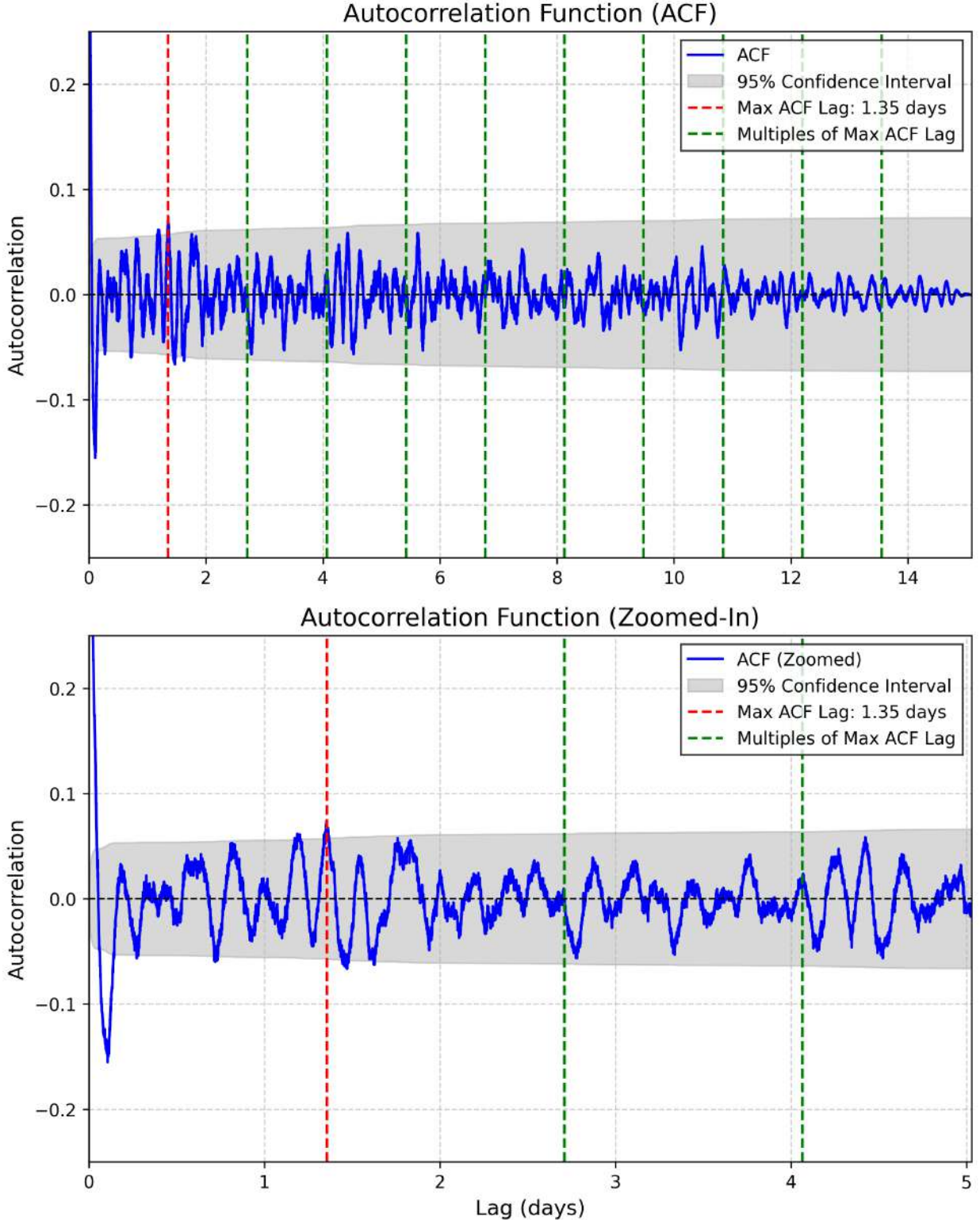


Figure 19: Autocorrelation function (ACF) of the SPECULOOS data of SP0314+1603. The top panel shows the full ACF up to 15 days, while the bottom panel zooms into short-term lags. The red dashed line marks the primary ACF peak beyond 0.1 days (lag = 1.35 days), and the green dashed lines show integer multiples. The shaded region indicates the 95% confidence interval.

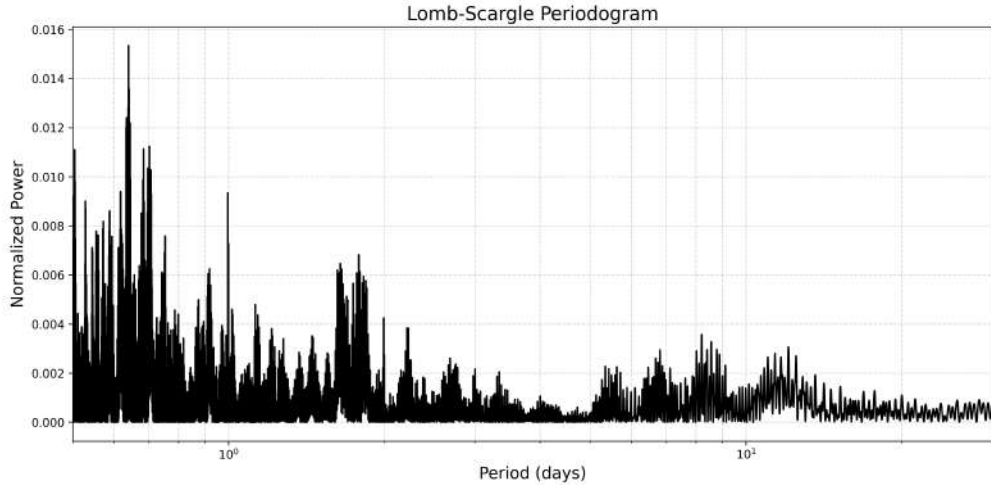


Figure 20: Lomb-Scargle periodogram of the photometric time series, showing significant power at 0.64 days.

4.4.3 Sinusoidal Modeling of Stellar Variability

As an initial attempt to model the stellar variability of SP0314+1603, a sinusoidal model was fitted to the photometric data. The model is defined by:

$$y(t) = F_0 + A \cdot \sin(2\pi ft + \phi) + \varepsilon \quad (18)$$

where $y(t)$ is the flux at time t , A is the amplitude of the sine wave, $f = \frac{1}{P}$ is the frequency (with period P), ϕ is the phase, F_0 is the constant baseline and ε is the offset, allowing for vertical shifting of the curve to account for nightly flux offsets.

To fit the model to the light curve, we minimize the following custom loss function:

$$\mathcal{L} = \sum_i (y_i - y_{\text{model}}(t_i))^2 + \lambda \sum_j \varepsilon^2, \quad (19)$$

where the first term is the residual sum of squares between the model and observed flux over all time points i , and the second term is a regularization penalty on the nightly offsets. The parameter λ controls the strength of the regularization and helps to avoid overfitting the offsets, ensuring that the model does not compensate for variability with arbitrarily large night-to-night shifts.

Initial guesses for the model parameters were informed by the standard deviation of the flux (for amplitude) and the dominant peak in the ACF (for period). The model was fitted on a night-by-night basis. For each subsequent night, the best-fit parameters from the previous night were used as initial values to refine and guide the process.

To probe variability on nightly timescales, we first focused on 11 nights of observations from the SAINT-EX telescope spanning 18 days. After preprocessing and relative normalization, we constructed a global light curve while preserving night-to-night flux offsets.

Figure 21 shows the nightly sinusoidal fits, with gray points representing the observed data, while the red line represents the best-fit model. The flux exhibits both larger-scale variability and shorter, potentially transit-like features embedded within, clearly illustrating the aforementioned challenges associated with this dataset.

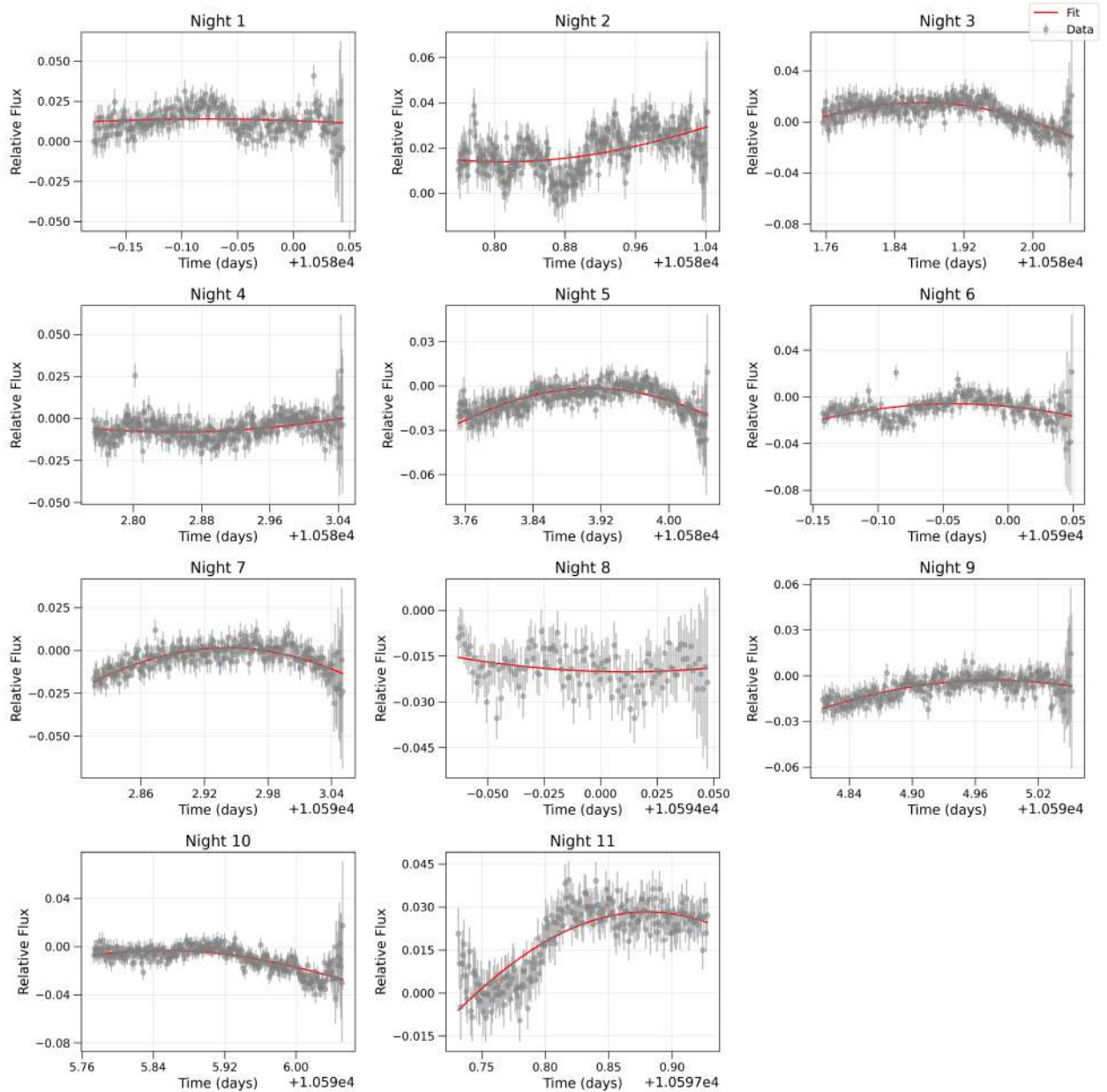


Figure 21: Fitted sine models for SAINT-EX observations. Gray points represent the observed data, the red line represents the best-fit model. The time axis is given in BJD - 2450000.

The model captures variability on the timescale of a night, while shorter-timescale features, such as potential planetary transits with durations of 0.05 days, remain unaffected. The evolution of the best-fit amplitude, period, and offset is shown in Figure 22. Note that a negative amplitude is mathematically equivalent to a positive amplitude with a phase shift of π .

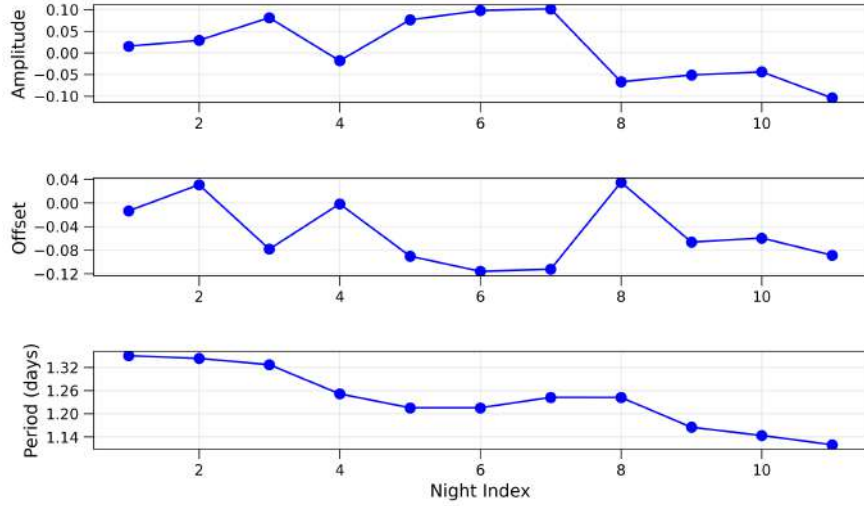


Figure 22: Sine-Fit: Evolution of the amplitude, offset, and period over the 11 nights of SAINT-EX observations of SP0314+1603.

The temporal variability in these parameters suggests that the stellar signal is not strictly periodic. Applied to the 11-night SAINT-EX dataset, the sine model reduced the root-mean-square (RMS) scatter of the light curve by 55.1% (from 0.015 to 0.0065). This substantial reduction reflects the effective removal of the dominant periodic signal as well as correction for inter-night flux offsets, all while preserving short-duration variability potentially consistent with planetary transits.

To generalize this method, the model was applied to the full photometric dataset, incorporating observations from all SPECULOOS telescopes. Figure 23 shows the temporal evolution of the fitted sine parameters across the complete observational baseline.

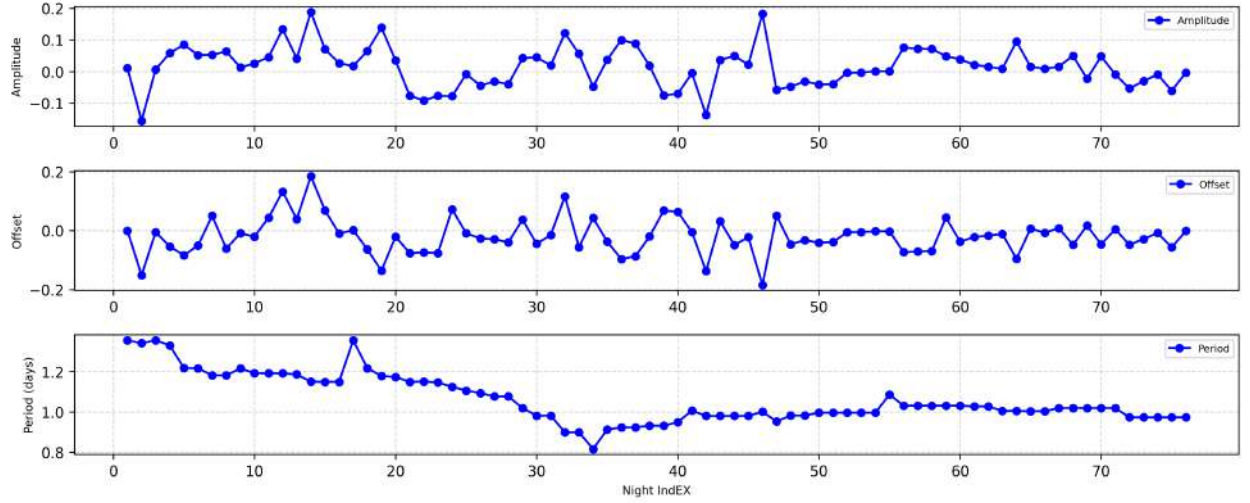


Figure 23: Sine-FIT: Evolution of amplitude, offset, and period for the full SPECULOOS dataset of SP0314+1603.

For the complete dataset, the sine model achieved an 18% reduction in RMS scatter (from 0.0068 to 0.0056). The smaller improvement compared to the SAINT-EX subset is expected, as nightly light curves were individually normalized (per night), reducing the overall scatter prior to modeling. But as with the SAINT-EX

subset, the parameters exhibit significant variation across nights, further reinforcing the non-stationary nature of the stellar variability. This behavior is likely indicative of evolving active regions or surface features modulating the observed flux.

To investigate whether any residual periodic transit-like features remain, a BLS analysis was performed on the model-subtracted residuals. The BLS periodogram and corresponding phase-folded light curve are shown in Figure 24.

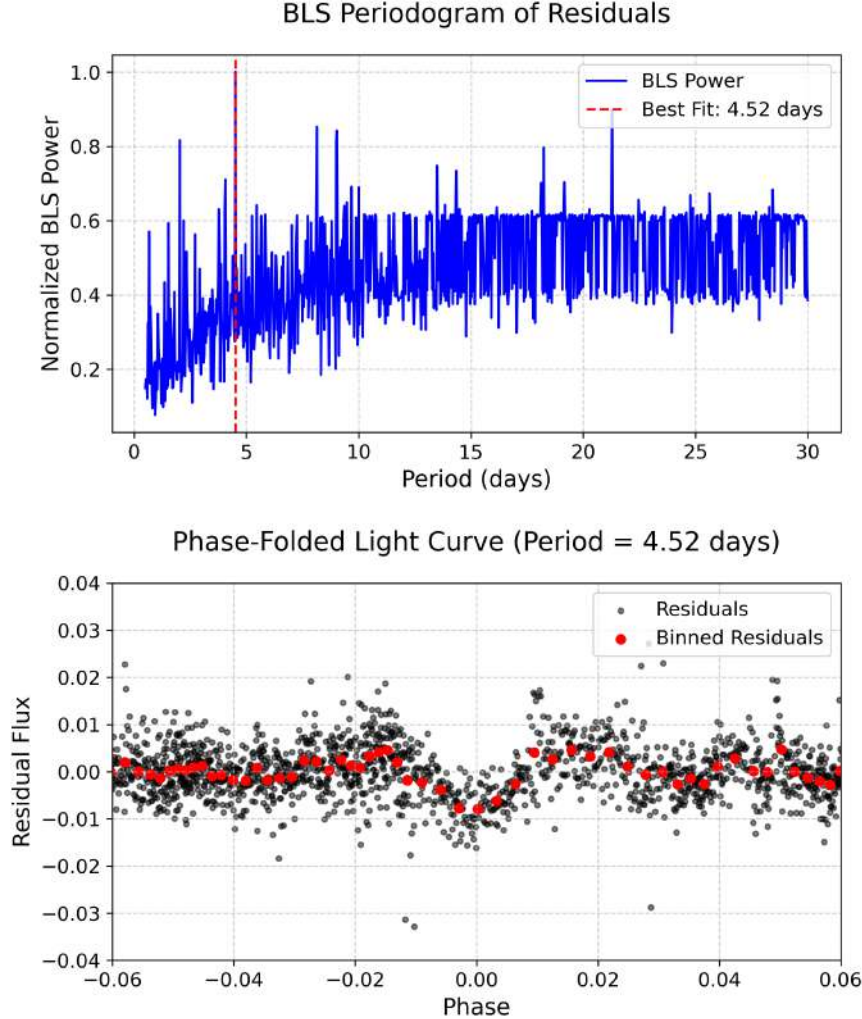


Figure 24: BLS periodogram (top) and phase-folded light curve for the residuals of the sine fit on the SPECULOOS observations of SP0314+1603.

The BLS identified a candidate signal with the following parameters: period $P = 4.516$ days, transit time $t_0 = 8846.403$ (BJD), duration = 0.05 days, and depth = 0.007. While the depth and duration are broadly consistent with the original transit-like feature detected in the raw data, the ephemeris is inconsistent with prior findings. Given the low, not significant SDE of this signal, it is more likely caused by quasi-periodic stellar variability or residual systematics, rather than an actual planetary transit.

To evaluate the effectiveness of the model and the nature of residual variability, we computed the ACF of the residual light curve (Figure 25).

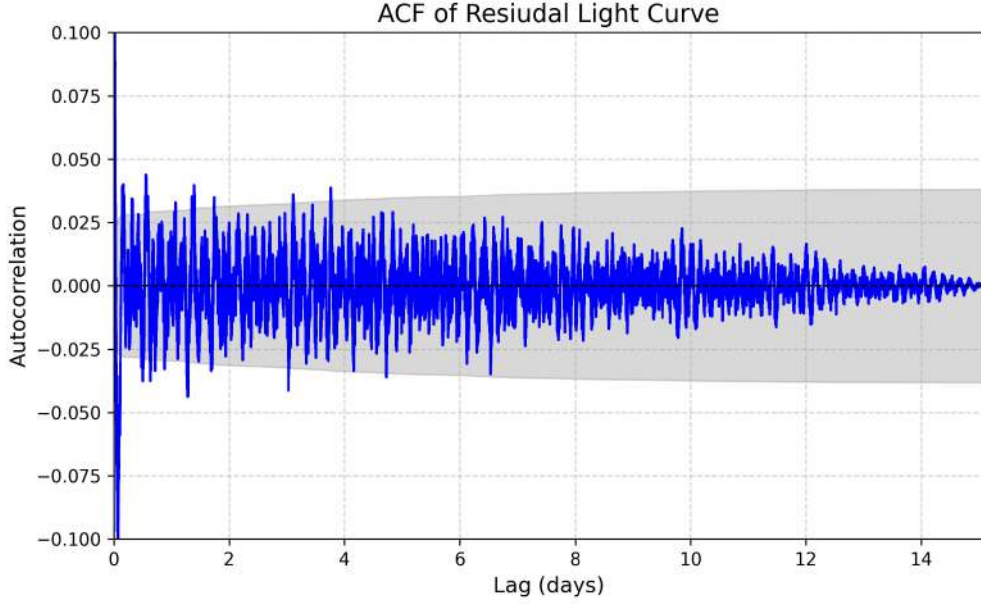


Figure 25: Autocorrelation function (ACF) of the residual light curve from the sine-fit applied to the full SPECULOOS dataset of SP0314+1603. The shaded region marks the 95% confidence interval.

The residual ACF reveals a reduced level of autocorrelation compared to the ACF of the original dataset (Figure 19), indicating that the sine-fitting process removed a dominant component of the quasi-periodic variability. However, the remaining peaks in the ACF still appear disordered and diffuse over longer timescales, suggesting that the underlying variability is more complex than a sinusoidal model can capture.

While an iterative approach combining ACF analysis and sinusoidal fits could theoretically extract additional periodicities from residual light curves, initial tests showed this method failed to capture meaningful variations and provide new insights. This approach also presents significant drawbacks, including computational inefficiency and the risk of introducing artificial patterns through repeated fitting. Given these limitations, we instead employ more robust Gaussian Process modeling in the following section to effectively separate stellar variability from transit signals.

4.5 Gaussian Process

We employ a Gaussian Process (GP) framework in attempt to model correlated variability in the light curve. Unlike the sinusoidal models used previously, GPs provide a flexible, non-parametric approach that does not assume a fixed functional form. Instead, they define a distribution over possible functions governed by a covariance kernel, allowing the data to inform the structure of the model. As noted by [Roberts et al. \(2013\)](#), GPs are particularly effective for capturing correlated noise arising from stellar activity and instrumental systematics.

In the previous section, the assumption was made that the correlated noise of the light curve could be explained by a parametric model (a sinusoidal one), thus limiting the (potentially infinite) space of functions explaining the variability. Despite the term "non-parametric", a GP is still governed by a set of hyperparameters that refine the distribution of the functions rather than defining an explicit functional form. The core of a GP is the covariance kernel function, which determines how data points influence one another.

In this analysis, we use a composite kernel combining two components: a damped Simple Harmonic

Oscillator (SHO) kernel and a Matern kernel with $\nu = \frac{3}{2}$, as implemented in the `celerite` package (Foreman-Mackey et al., 2017). This combination allows to model both the quasi-periodic nature of stellar rotation and the evolving, longer-term trends associated with active region lifetimes. The additive nature of the kernel ensures the resulting covariance function remains valid. The model is defined by five hyperparameters: S_0 , ω_0 , Q , σ and ρ .

To initialize the model, we adopt physically motivated estimates for these hyperparameters. The characteristic frequency ω_0 is derived from the dominant peak in the ACF of the light curve, using:

$$\omega_0 = \frac{2\pi}{P_0}, \quad (20)$$

where P_0 is initialized as the value of the strongest ACF peak.

The quality factor Q reflects how many oscillations occur before the signal is significantly damped. Based on the observed decay in the ACF we set $Q = 3$, as the multiples of the primary ACF peak remain aligned with local maxima for approximately three cycles. This choice, however, remains a qualitative estimate.

The amplitude is estimated from the observed variance in the flux (Foreman-Mackey et al., 2017).

The hyperparameter σ of the Matern kernel, which represents the overall variability amplitude, was initially set to the standard deviation of the flux, providing a measure of the total variability in the light curve.

The parameter ρ , which defines the correlation length (i.e., how quickly or slowly the variations evolve), was initially set to 2 days, to capture longer-term variations.

Once the model is defined, we construct the log-likelihood function and use Markov Chain Monte Carlo (MCMC) sampling via the `emcee` package to explore the posterior distribution of the hyperparameters. Priors are placed on the hyperparameters to guide the model and incorporate prior knowledge. The corresponding code setup for the MCMC implementation is displayed in Appendix B. The median values from the posterior samples are adopted as the best-fit parameters.

Although the initial values are based on estimates, the model is designed to be flexible enough to converge to a well-constrained solution. Our primary goal is not precise constrain the hyperparameters, but rather a faithful reconstruction of the underlying variability structure. Hyperparameters were sampled in log-space to enforce positivity and enhance sampling efficiency. For the initial sample of hyperparameters the following, broad set of priors was used, shown in Table 8. In addition, a constraint was applied to ensure that $\log \rho$ remained positive, since we want to model long-timescale variability (greater than one day) using the Matern Kernel. These priors were intentionally wide to allow the data to speak for itself in this first exploratory stage. They were chosen to reflect plausible ranges without overly constraining the model. The results of the MCMC process are also listed in Table 8, the corresponding corner plot is shown in Figure 26.

Table 8: Initial Prior Distributions for GP Hyperparameters and corresponding Posteriors.

Parameter	Log-Space Prior	Log-Space Results
$\log(S_0)$	$\mathcal{N}(-9.95, 2)$	$11.95^{+0.54}_{-0.46}$
$\log(Q)$	$\mathcal{N}(1.1, 3)$	$-2.49^{+0.22}_{-0.23}$
$\log(\omega_0)$	$\mathcal{N}(1.54, 2)$	$4.66^{+0.19}_{-0.19}$
$\log(\sigma)$	$\mathcal{N}(-5, 3)$	$-0.82^{+0.07}_{-0.07}$
$\log(\rho)$	$\mathcal{N}(0.7, 2)$	$2.00^{+0.00}_{-0.01}$

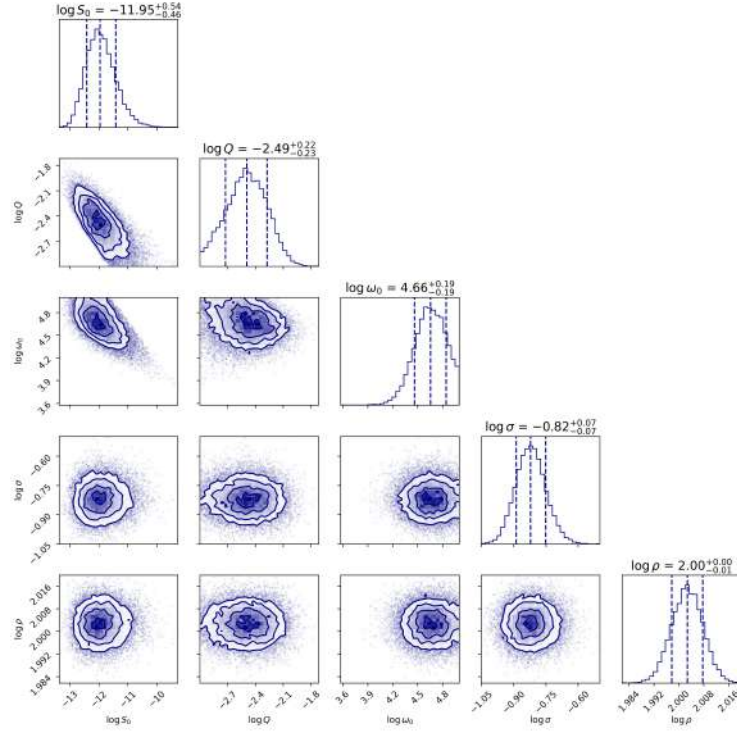


Figure 26: Corner plot showing the posterior distribution of initial set of GP hyperparameters.

Notably, the parameters $\log Q$, $\log \omega_0$, and $\log \sigma$ show posterior peaks that lie outside the one-sigma region of their respective gaussian priors. This indicates a strong likelihood signal in the data for these parameters and suggests that, while the initial priors were broad, the data provided sufficient information to constrain the model. We also tested narrower Gaussian priors. This did however not result in an improved fit.

An example of the resulting GP fit using the initial hyperparameter estimates is shown in Figure 27. The observed data from the night is plotted alongside the GP model. The residuals (observed flux minus model prediction) do not show visible systematics, suggesting that the GP successfully captures the dominant correlated variability in the data.

The ACF of the residual flux from the GP model of the full dataset is shown in Figure 28. It shows no clear remaining structure, indicating that the model has effectively removed most of the correlated noise, particularly on longer timescales.

The key challenge in this approach is overfitting. If the model is too flexible, it absorbs all variations in the data, potentially removing real transit signals. This can be seen in Figure 27, where the initial transit candidate (first panel) is completely absorbed and no longer present in the residual flux.

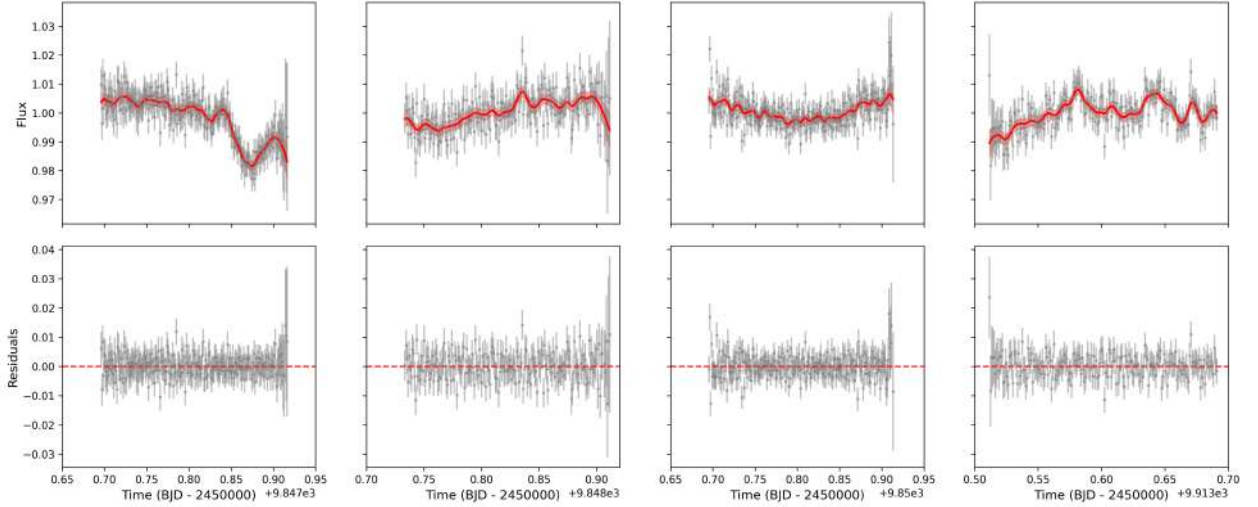


Figure 27: Gaussian Process regression applied to the light curves. Top: observed flux (gray points) with the best-fit GP model (red line) and 1σ uncertainty (shaded region). Bottom: residuals after subtracting the GP model, with the dashed red line indicating zero flux.

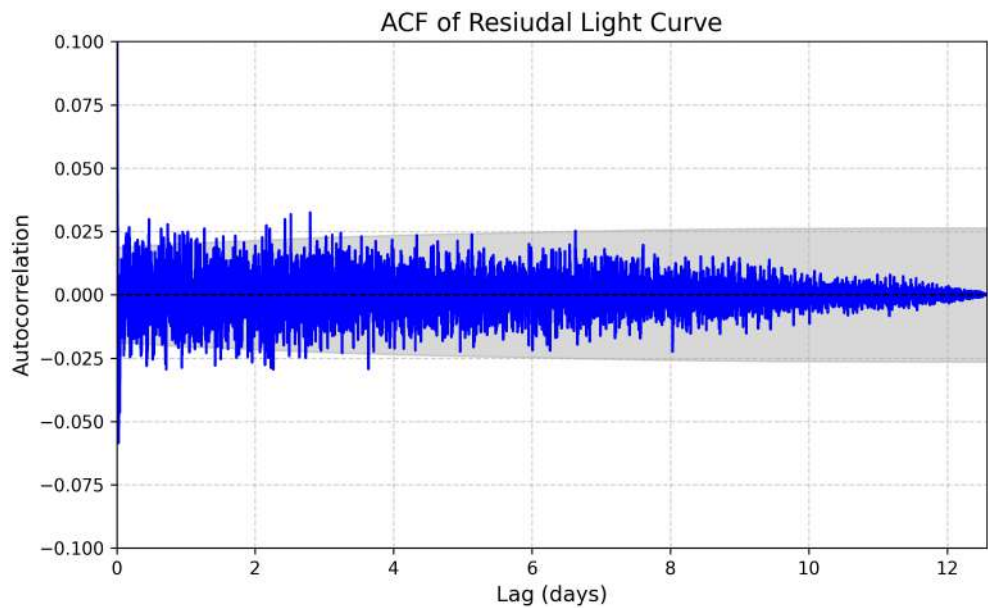


Figure 28: Autocorrelation function (ACF) of the residuals after initial GP modeling.

4.5.1 Refining Hyperparameters Using Injected Transits

Since the initial selection of hyperparameters did not preserve the initial transit candidate, a more iterative, trial-and-error approach was adopted. To guide this refinement process, synthetic transits were injected into the light curve to test the GP model's ability to preserve real transit signals. A planetary transit model was generated using the `batman` package (Kreidberg, 2015), incorporating parameters based on the best-fit planetary transit model from the MCMC fit (see Section 4.3). This model was then multiplied with the observed flux, simulating the presence of a planetary transit in the data. The process then involved refining both the initial guesses and prior distributions of the hyperparameters. Various combinations were tested to identify a model that preserved the injected transits in the residuals while still removing a substantial amount of the correlated noise.

Figure 29 presents three examples of GP modeling applied to a night with an injected transit. The first two GP models exhibit clear overfitting, fully absorbing the transit signal, such that it is not present in the residual flux. In contrast, the third model successfully captures the larger flux variations around the transit while leaving the transit itself intact. To further evaluate model performance, the root mean square (RMS) of the residuals was analyzed.

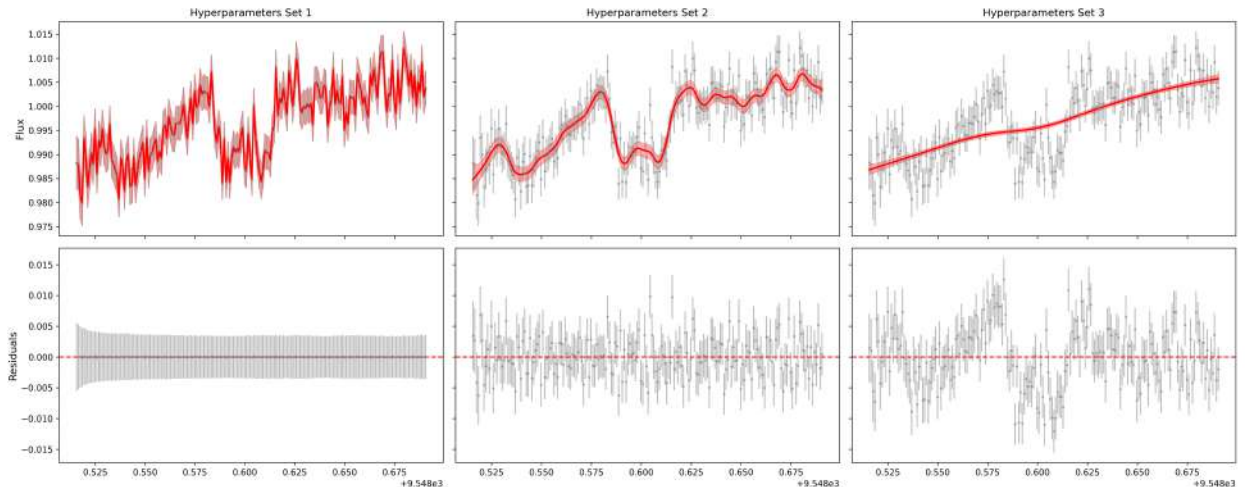


Figure 29: GP fit with injected transit signals for different hyperparameter sets.

Further experiments were conducted using a covariance function composed of the sum of two SHO kernels. However, this configuration did not yield an improvement over the combination of a single SHO and a Matern Kernel. A comparative analysis of the residual RMS confirmed that the SHO + Matern setup was more effective at suppressing stellar variability while retaining transit signals.

4.5.2 Optimized GP Model

Table 9 displays the best-fit values of GP hyperparameters from the final MCMC sampling and Figure 30 shows the MCMC posterior distributions for the final GP. The linear values indicate, that the GP describes a process with low characteristic frequency (i.e., high period) and a strong damping. While MCMC is expected to converge to well-defined posteriors, we find that $\log(\sigma)$ converges toward the upper bound of its prior (towards less negative values). This implies a preference for larger amplitudes, potentially compensating for the restricted GP flexibility, mainly in short-timescale variability. The constrained hyperparameter space forces the GP to model only larger-scale variability while preserving transits in the residuals. This behavior

indicates that our constraints effectively shape the GP behavior, though further refinement of priors or kernel selection may enhance robustness.

Table 9: Median best-fit values of GP hyperparameters from the final MCMC sampling.

Parameter	Log-Space Value	Linear Value
S_0	-4.998	6.75×10^{-3}
Q	-0.242	0.785
ω_0	0.009	1.009
σ	-1.571	0.208
ρ	0.875	2.399

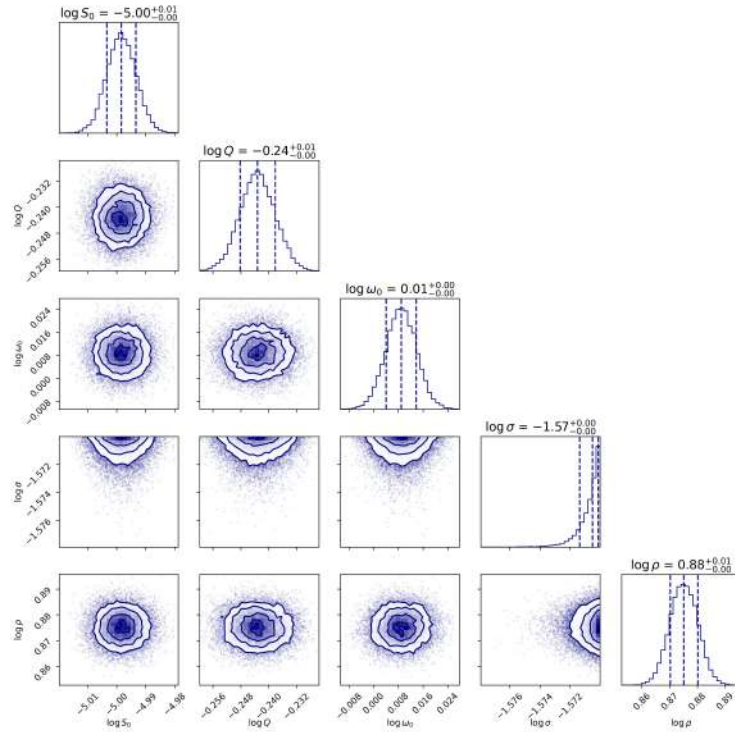


Figure 30: Corner plot of the final, optimized posterior distribution of GP hyperparameters.

Returning to the original dataset without injected transits, the final GP model was applied using the optimized set of hyperparameters. The GP achieved a 33% reduction in RMS scatter from 0.0068 to 0.0046 in the residual flux. This improvement is significantly greater than that achieved by the sine model (18%), highlighting the GPs enhanced ability to capture the quasi-periodic and evolving nature of the stellar variability.

Figure 31 shows the GP fit for the night of the initial transit candidate (first column), along with three subsequent nights. As shown, the transit-like signal remains clearly visible in the residual flux.

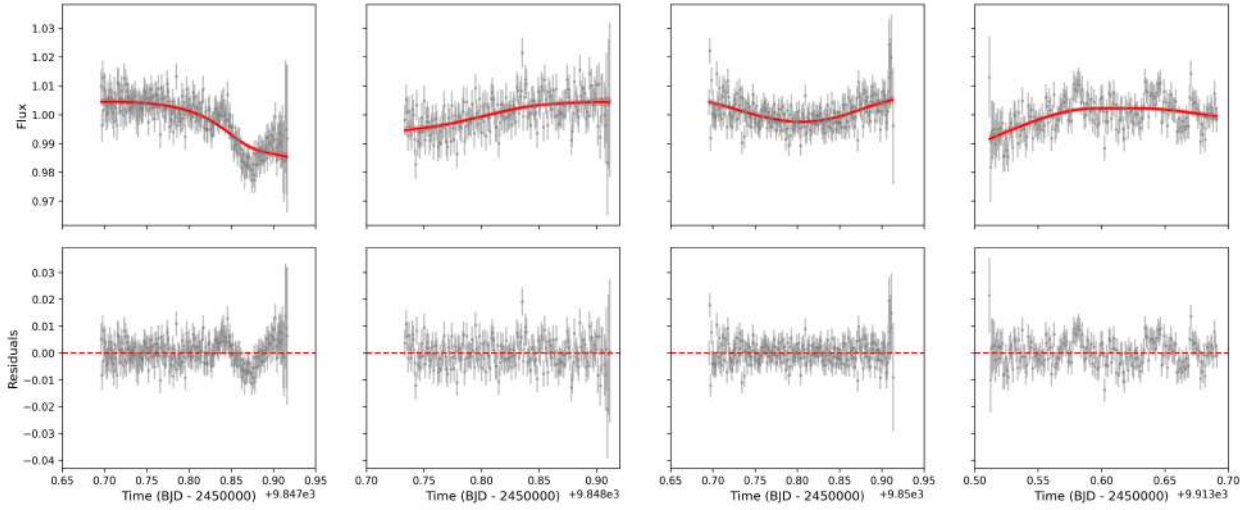


Figure 31: GP fit (first row) and residuals (second row) for selected nights. The first night includes the initial transit candidate

The ACF of these residuals was evaluated, shown in Figure 32. Compared to the original ACF in Figure 19, the residuals no longer exhibit strong structure over longer timescales, suggesting that the large-scale correlated variability has been effectively removed. Some weaker residual autocorrelation may still be present, primarily on shorter timescales. As before, the significance levels indicated by the 95% confidence interval should be interpreted with caution. This interval may underestimate the true uncertainty in the presence of time-correlated noise, leading to false indications of significance.

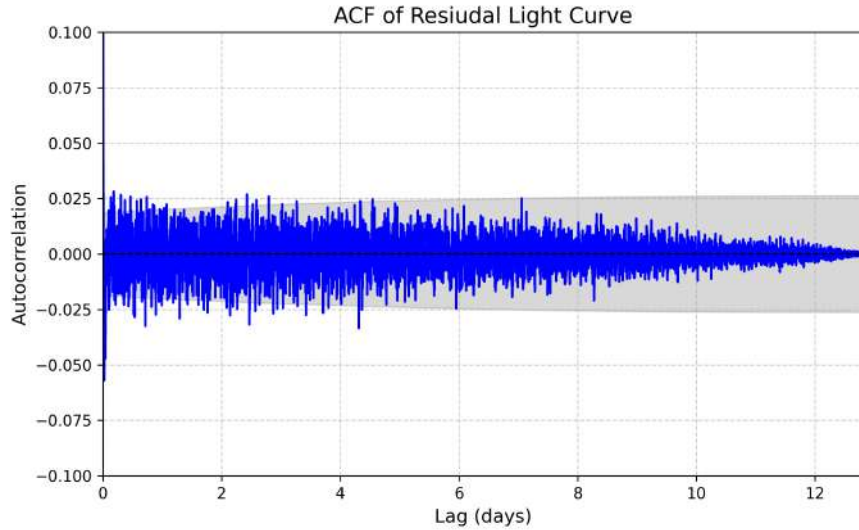


Figure 32: ACF of the residual light curve after applying the optimized GP model.

Both the amplitude and coherence of the ACF are reduced compared to the original ACF (Figure 19) and the one after the sinusoidal model (Figure 25). This suggests that the GP model has better captured the underlying variability, resulting in residuals that more closely resemble uncorrelated noise.

The improved performance of the GP model can be attributed to its flexibility. Unlike the sinusoidal model, which enforces a rigid functional form, the GP can adapt more freely to the complex and evolving

patterns present in the data, thereby avoiding the introduction of artificial structure into the residuals.

4.5.3 BLS on Residual Flux

A BLS periodogram was applied to the residual flux from the optimized GP model. The resulting periodogram is shown in Figure 33.

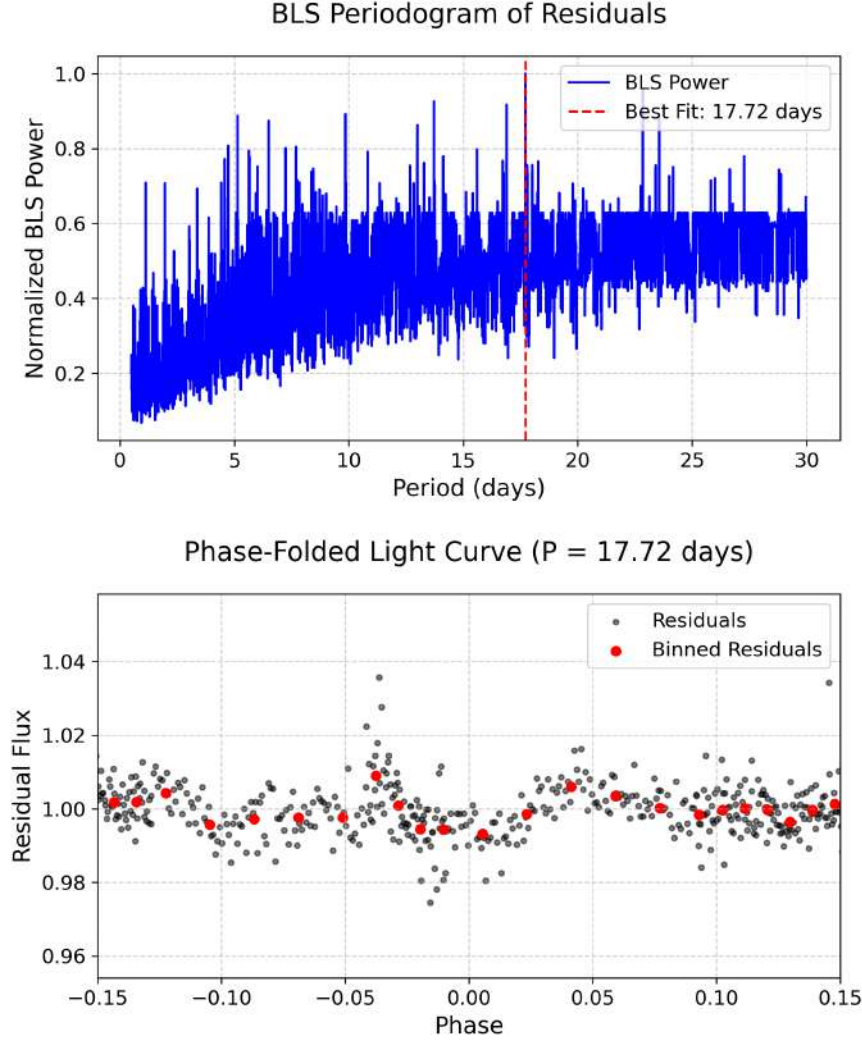


Figure 33: BLS periodogram (top) and phase-folded light curve for the residuals of the GP fit across all observations of SP0314+1603.

Once again, the BLS analysis fails to reveal a dominant peak corresponding to a convincing periodic signal associated with the initial transit candidate, both in shape and ephemeris. Visual inspection of the identified features suggests that they are more likely residual systematics rather than genuine transit events. The SDE falls well below the significance threshold. This strongly suggests that, if transits are indeed present in the dataset, the BLS method is not well-suited for detecting such shallow signals in the presence of residual variability. At this stage, the BLS does not offer additional insight. We therefore proceed with a more direct approach to exploring potential periodicities.

4.5.4 Visual Inspection of Residual Flux

Through visual inspection of the residual flux from the optimized GP model, 13 patterns were identified as potentially transit-like. To ensure these patterns were genuine and robust, they were also separately detrended using the approach described in Section 4.4.1. This additional step helped confirm that the features remained consistent, further validating their presence and confirming their authenticity. Figure 34 shows the residual flux for four representative events; the full set of visually identified candidates is presented in Appendix C (Figure 41).

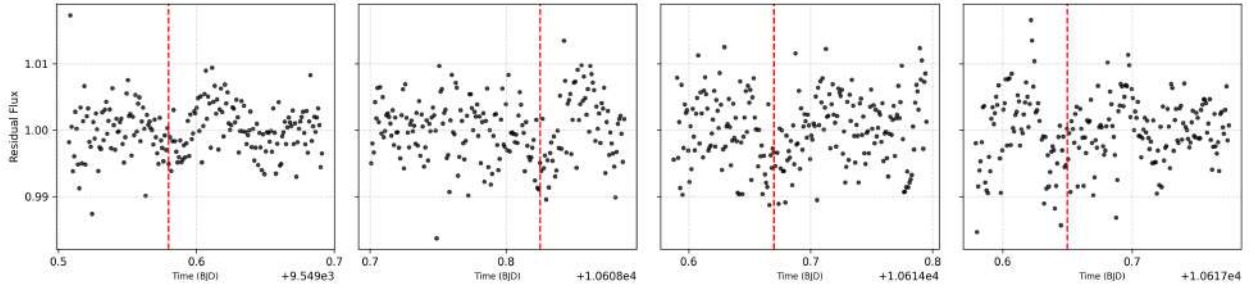


Figure 34: Residual flux for four selected transit-like patterns, determined through visual inspection. The red dashed line indicates the potential mid-transit time for each night.

To investigate potential periodicity among these events, a custom period-search algorithm was implemented. The algorithm tested candidate orbital periods ranging from 5 to 50 days in steps of 0.01 days, assessing alignment with the visually identified transit times. Each transit was allowed a temporal uncertainty of ± 0.01 days. A period was considered viable if it predicted multiple transit events, including the initial candidate at $t_0 = 9847.87$ BJD. Periods shorter than 5 days (and larger than 50 days) were excluded, consistent with the constraints derived from the MCMC fit (see Figure 18).

Several candidate periods were found to satisfy these criteria, each matching at least two apparent transit features while not being excluded by the available data. These are summarized in Table 10.

Table 10: Candidate orbital periods consistent with at least two visually identified transit events. Boldface indicates the favored period.

Periods (days)
7.65, 7.85, 8.52, 8.73, 9.28, 9.30, 10.80, 11.89, 12.78, 13.12, 14.27, 15.70, 16.49, 16.91, 17.04, 18.56, 19.17, 19.69, 21.30 , 21.38, 22.01, 23.27, 23.78, 25.56, 26.24, 28.51, 28.54, 29.83, 34.99, 35.71, 38.34

Notably, only one period, **21.30** days, aligned with three of the identified events and remained compatible with all available observations, making it the most promising candidate. Figure 35 shows the residual flux around the predicted transit times for this ephemeris. Importantly, the 21.30-day period also lies well within the boundaries of the period posterior distribution obtained via the MCMC fit of the single transit candidate (see Figure 18). Harmonic fractions of this period ($\frac{P}{2}$ and $\frac{P}{3}$) were also tested, but ruled out, as they predicted transit events during nights where no such features were present. The patterns at predicted transit events for these two harmonic periods can be found in Appendix C (Figures 42 and 43).

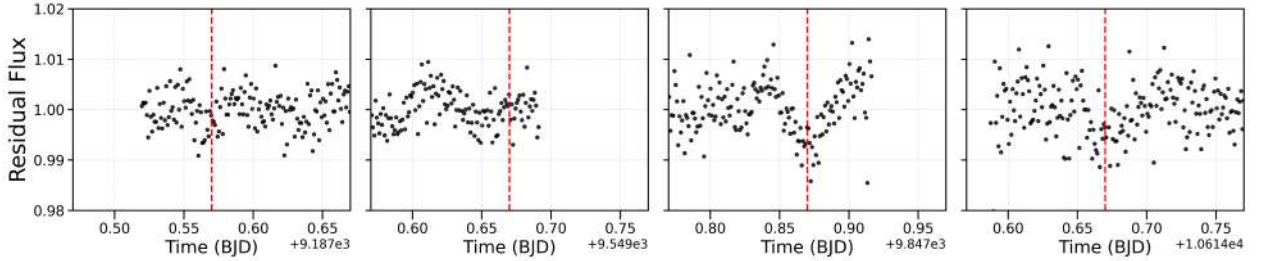


Figure 35: Residual flux centered on predicted transit times for an ephemeris of $t_0 = 9847.87$ BJD and $P = 21.30$ days.

4.5.5 Folded Light Curve

As a next step, the light curve was phase-folded using the candidate period of 21.30 days. The resulting light curve is shown in Figure 36. A clear dip is visible around the predicted transit center, supporting the plausibility of this period and motivating further analysis.

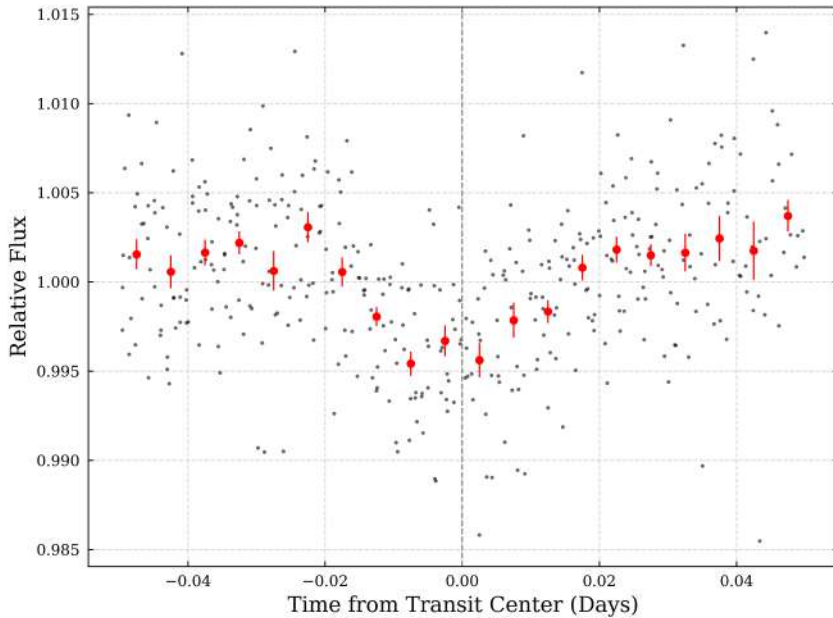


Figure 36: Folded light curve using a trial period of 21.30 days. Individual flux measurements are shown in black, with red points indicating binned flux values and associated uncertainties. The vertical dashed line marks the expected transit center.

In addition to folding strictly based on the trial period, an alternative alignment was tested by manually adjusting the phase of individual events. A slight shift of the transit center near BJD 9549 led to a marginally improved visual alignment.

As a next step, the folded light curve was modeled using an MCMC algorithm, following the same procedure applied to the initial transit candidate (see Section 4.3). The same set of priors from Table 6 was used, with two modifications: the mid-transit time t_0 was set to 0, and a Gaussian prior centered on the candidate period was added, $\mathcal{N}(21.30, 0.1)$ days. The resulting transit fit is shown in Figure 37, and the corresponding posterior distributions are presented in Figure 38. Convergence of the parameters was ensured

using the \hat{R} statistic introduced by [Gelman & Rubin \(1992\)](#).

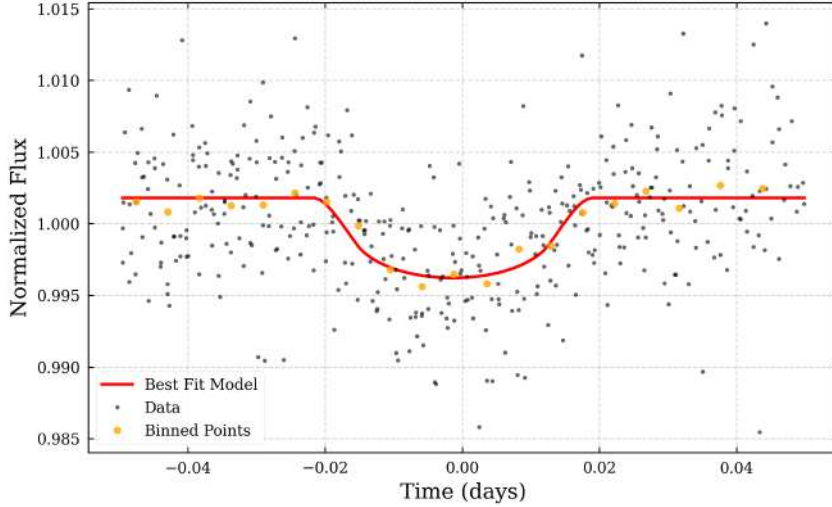


Figure 37: Transit light curve fit to folded data of matching patterns. The black points represent the individual flux measurements, while orange points show binned data (15-point bins) for visual clarity. The red curve represents the best-fit transit model derived from the MCMC posterior.

The resulting parameters from the model fit are listed in Table 11.

Table 11: Results of the MCMC fit for SP0314+1603.

Parameter	Result
Mid-transit time (t_0)	$-0.001^{+0.001}_{-0.001}$ (BJD _{TDB})
Orbital period (P)	$21.305^{+0.097}_{-0.096}$ (days)
Radius ratio (R_p/R_\star)	$0.077^{+0.004}_{-0.004}$
Impact parameter (b)	$0.796^{+0.023}_{-0.025}$
Limb-darkening coefficient (u_1)	$0.638^{+0.097}_{-0.099}$
Limb-darkening coefficient (u_2)	$0.315^{+0.095}_{-0.094}$
Baseline Flux (F_0)	$1.002^{+0.0003}_{-0.0002}$
Stellar density (ρ_\star)	$73574.277^{+6140.83}_{-6265.43}$ (kg m ⁻³)
Transit duration (T_{dur})	$0.0391^{+0.00169}_{-0.00082}$ (days)

This would correspond to a planet of 0.899 ± 0.06 Earth radii. The scaled semi-major axis is calculated to be $\frac{a}{R_\star} = 123.13 \pm 3.19$ and the inclination $i = 89.63^\circ \pm 0.09^\circ$. The reduced uncertainty in $\frac{a}{R_\star}$ is consistent with the narrower range of orbital periods, compared to the initial single-candidate analysis.

The fit shows a reasonable agreement with the data. The corresponding corner plot (Figure 38) shows well-converged and constrained posterior distributions. However, in comparison to the initial transit candidate, the depth is notably shallower, resulting in a smaller radius ratio R_p/R_\star . The derived duration is also shorter than in the initial fit (see Table 7). Potential explanations and limitations are discussed in the following section.

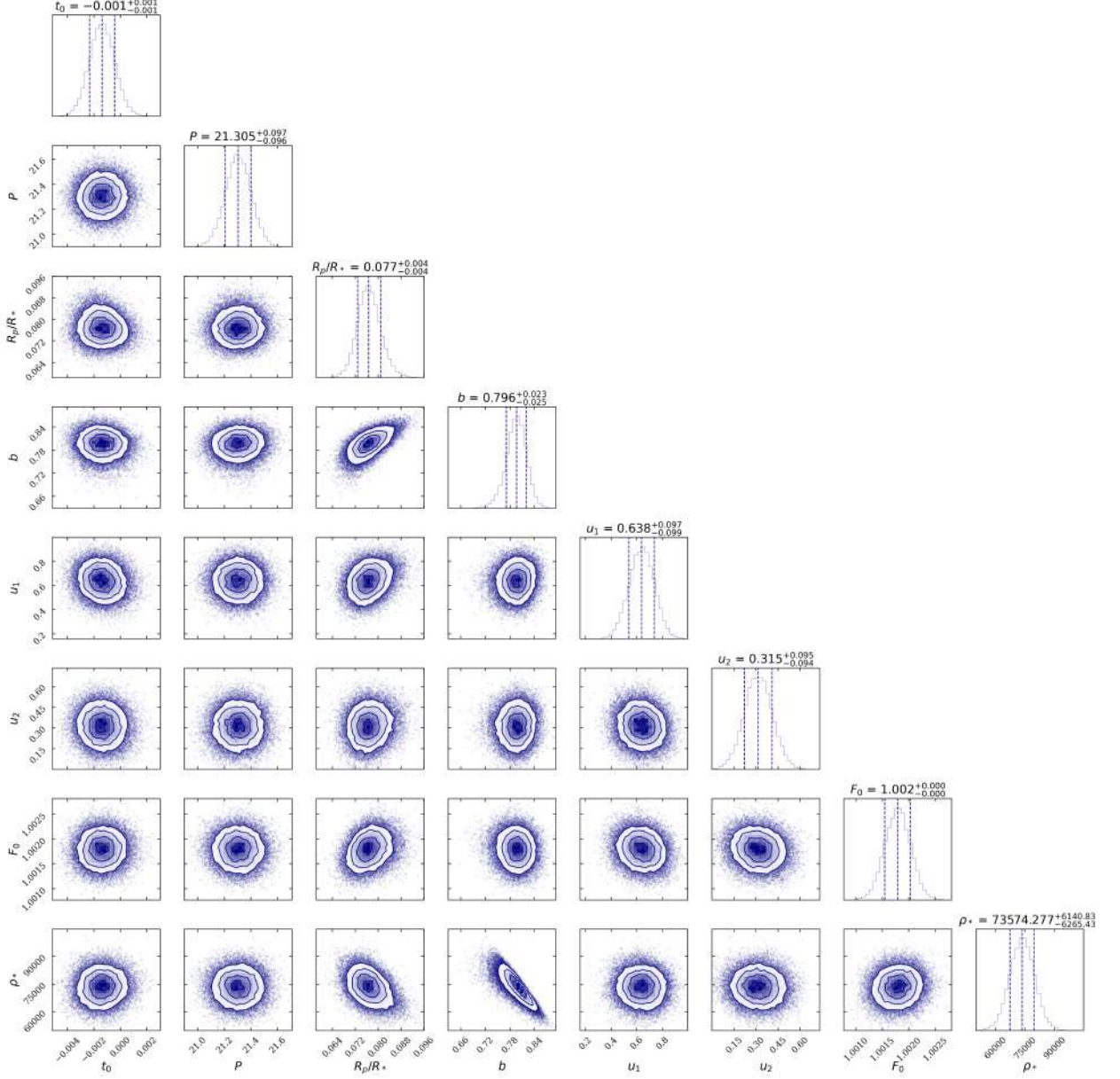


Figure 38: Corner plot showing the posterior distributions of the fitted parameters from the MCMC fit of the folded light curve. The solid lines in the 1D histograms represent the median values, and the dashed lines indicate the 16th and 84th percentiles (1σ credible intervals).

4.5.6 Discussion and Limitations of This Approach

While the transit-like signals in the residuals show a decent degree of alignment for a 21.20-day period across the multiple epochs, several important limitations should be considered.

First, although the MCMC fit shown in Figure 37 appears to model the data well and the posterior distributions show acceptable convergence (see Figure 38), the posterior on the period remains relatively broad, with an uncertainty of ± 0.09 days. This is notable, as a Gaussian prior was imposed on the period, and such a broad posterior suggests that the fit is driven more by the prior than by strong empirical constraints from the data. In other words, the model likely did not converge on a well-defined period based purely on the observed data. Additionally, the MCMC fit on the folded data was repeated using a weaker and no prior on the period. This approach was also not able to constrain the period more. This failure calls into question the robustness of the detection and may reflect either insufficient signal-to-noise in the data or a more complex underlying variability not consistent with a transit profile.

Another important consideration is the variation in depth and duration in the folded light curve compared to the initial candidate. This raises the possibility that these signals may not come from the same coherent source. It is also possible that the GP, despite careful tuning, may have been too aggressive and still suppressed the depth of some transit-like features. Additionally, the detrending applied to the initial candidate prior to the MCMC fit might have introduced subtle biases to the data, which could further contribute to the discrepancies.

It has to be noted, that the quality of the photometric data also varies substantially between nights, which could affect the apparent depth and shape of the transit features. For context, the out-of-transit RMS scatter per night were 3163 ppm (BJD 9187), 3293 ppm (BJD 9549), 4635 ppm (BJD 9847), and 4799 ppm (BJD 10614). Differences in observing conditions, signal-to-noise ratio, and instrumental systematics would likely influence the apparent morphology of the transit features.

Another point of uncertainty is the potential timing offset in the pattern near BJD 9549. If the adopted period is slightly incorrect, such an offset naturally arises. The discrepancy is consistent with the propagation of a small period uncertainty. Even a minor period error of just 0.001 days (1.44 minutes) leads to a cumulative offset of 0.014 days after 14 cycles (the event at BJD 9549 occurs $N = 14$ cycles after the reference transit at BJD 9187.57), based on the relation $\Delta t = N \cdot \Delta P$. This may indicate that the true orbital period slightly deviates from the tested value of 21.30 days. The executed period determination remains a relatively rough approach.

A potential explanation for a misalignment might also be that the periodicity does not reflect a strictly constant orbital period. Small deviations, such as transit timing variations (TTVs) potentially caused by gravitational interactions with other bodies, or eccentricity of the orbit, can shift transit times across epochs (Agol et al., 2005; Holman & Murray, 2005). These effects could make it harder to detect a clean, repeated signal when folding the data.

It is also worth noting that the transit-like events are separated by significant time spans: approximately 362, 300, and 767 days span between the four candidate transits. These long baselines amplify the effect of even small uncertainties in period and increase the challenge of phase alignment.

Additionally, short-timescale stellar variability may still be present and could distort or mimic shallow transits. Residual systematics or stellar variability that was not fully removed by the GP model could potentially still be masking a real planetary signal. Given these limitations, greater emphasis is placed on the phase-folded light curve, which benefits from increased signal-to-noise through the combined data.

Taken together these considerations, it cannot be ruled out, that the light curve in Figure 36 is only a

chance alignment of uncorrelated patterns. It is also possible that the original event has a different orbital period, maybe one of those listed in Table 10. A definitive conclusion cannot be drawn. The phase-folded light curve (Figure 36) still exhibits a transit-like shape, and the model fit is consistent with a planetary object. While the evidence is insufficient to confirm a planetary origin, it is also not conclusive enough to rule one out.

4.5.7 Outlook

Despite the limitations outlined above, the 21.30-day candidate period remains worth pursuing.

Moving forward, there are a few directions that can be taken. Additional observations at predicted transit times would be the most direct way to test the periodicity. Confirming whether the signal repeats consistently at the expected ephemeris of $t_0 = 9847.87$ BJD and $P = 21.30$ days would strengthen the case for a planetary origin. Conversely, continued evolution or disappearance of the signal would favor a stellar or instrumental cause.

In addition, the alternative candidate periods that align with only two of the identified patterns (Table 10), may also be worth investigating in more detail. These signals could represent unrelated transit-like events, additional components of a sparsely sampled multi-planet system, or simply manifestations of stellar variability.

As a possible next step, one could extend the MCMC model to include orbital eccentricity and compare the Bayesian Information Criterion (BIC) between the circular and eccentric fits. However, transit photometry alone provides limited constraints on eccentricity, particularly in cases of low signal-to-noise (small planets), so any results from such an analysis should be interpreted with caution (Price et al., 2015).

Finally, other methods, such as radial velocity measurements could provide valuable complementary evidence. This may help to either confirm the planetary nature of the signal or better characterize potential sources of false positives.

5 Sp0720-0846 - Scholz's Star

Sp0720-0846 of the SPECULOOS target list, also called Scholz's Star, is a M9.5+T5.5 binary at 6.8 pc (Sebastian et al., 2021; Scholz, 2014; Dupuy et al., 2019). It has been reported that the binary has passed through the solar system within at 52,000 AU of the Sun, approximately 70,000 years ago (Mamajek et al., 2015).

Observations of this target with SPECULOOS-affiliated telescopes revealed two separate transit-like events. The detrended data of these observations (same approach as in Section 4.1) are displayed in Figure 39, with potential transits around 2459197.775 and 2459224.650 BJD. The fact that this is a binary introduces further complexity in interpreting the observed signals, as this can affect both the timing and shape of transit events, making reliable detection difficult (Sybilska et al., 2010).

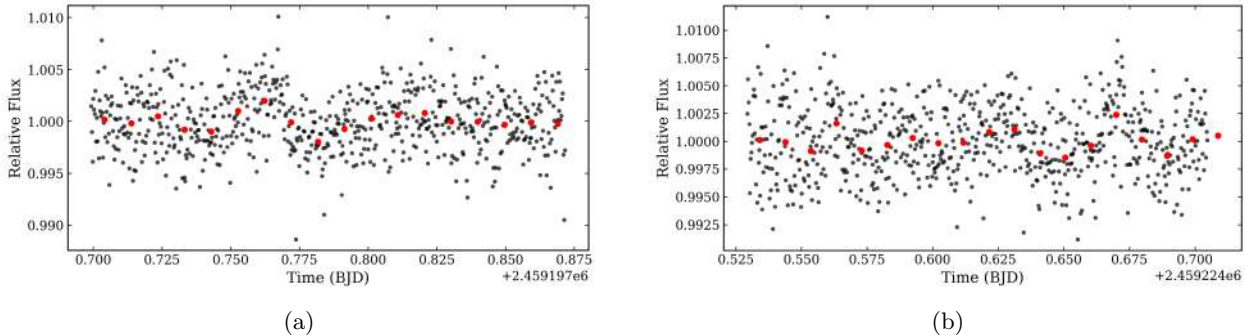


Figure 39: Detrended light curves showing two separate transit-like events observed in the Scholz's star system. Left: First event. Right: Second event.

An earlier analysis (prior to the work presented in this thesis) suggested several potential ephemerids for the transiting body: $9197.786 + N \ 4.4770 / 5.3724 / 6.7155 / 8.9540$ days.

To assess the observability of predicted transit events, the `astropy` (Astropy Collaboration et al., 2022) and `astroplan` (Morris et al., 2018) Python packages were used. The `astropy.time.Time` and `astropy.coordinates.SkyCoord` classes were used to define ephemeris-based timing and celestial coordinates of the target, while `astroplan.Observer` and `FixedTarget` enabled site-specific visibility checks from the San Pedro Martir Observatory (latitude: 31.0435° , longitude: 115.4548°).

The script evaluated a range of predicted mid-transit times for each ephemeris. For each event, a four-hour observation window (2 hours around the predicted transit midpoint) was tested for observability. Two main constraints were applied:

- **Altitude-Constraint:** Minimum target altitude of 27° above the horizon.
- **At-Night-Constraint:** Only times during astronomical night (i.e., Sun below -18°) were considered.

If the transit midpoint occurred within a time window where the target was observable under the defined constraints, the event was classified as observable.

Unfortunately, due to poor weather and unfavorable observing conditions, no conclusive follow-up detections were possible during the allocated windows. However, this target remains compelling and further observations are scheduled. Thus, the target will greatly benefit from future investigation of these observations.

6 Conclusion and Outlook

While the work presented in this thesis did not result in a conclusive exoplanet detection, it demonstrates a systematic, reproducible approach to analyzing light curves and investigating single transit-like events by combining ground-based observations with TESS data. Moreover, it strongly motivates continued follow-up analysis and observations. This outcome may not be the most definitive or satisfying in the classical sense, but it reflects the reality and challenges of working with complex observational data.

For **SP1036+1923**, which exhibited a single transit-like event in SAINT-EX data from 2024-03-13, a distribution of possible orbital periods for the potential planet could be constrained. First, an injection-recovery experiment was carried out. Given the large uncertainty in planetary and stellar radii, it cannot be conclusively determined whether the event would be detectable with TESS. The analysis strongly suggests, that a similar transit event with a period of ≤ 5 days would be detectable with TESS. The analysis of the TESS data however does not yield a detection, effectively ruling out periods ≤ 5 days for this candidate. Additionally, an MCMC fit of the transit pattern in the SAINT-EX data puts a further constraint on the period. The posterior distribution yields a median period of 11.0 days, with a 16th percentile of 6.67 days and an 84th percentile of 16.17 days. This provides a basis for further follow-up observations and analysis.

All available SPECULOOS data of this target were also inspected. The light curves exhibit photometric variability, with some patterns resembling potential transit events. However, these patterns vary in morphology and are surrounded by additional variability, suggesting stellar activity as a likely cause. It is still possible, however, that transits are embedded within the variability. As an exploratory step, periods within the aforementioned range were tested, and one candidate period of 13.148 days was found to match the SAINT-EX event and two additional potentially transit-like features while not excluded by other data. A clear limitation of this approach is the presence of variability near the identified signals, which may indicate stellar variability or instrumental systematics. Nevertheless, the 13.148-day period remains a compelling target for follow-up observations, which could either confirm or rule it out as the orbital period of a previously undetected exoplanet.

Target **SP0314+1603** showed a transit-like feature in the observations with the EUROPA telescope on 2022-09-24. The main challenge in this case stemmed from the shallow depth combined with strong photometric variability from the M9 host, which could obscure or mimic transit signals. An injection-recovery experiment using the TESS data indicated that the transit candidate would not be detected by TESS. The MCMC fit of the single transit-like pattern yielded a posterior period distribution with a median of 21.565 days, a 16th percentile of 12.01 days, and an 84th percentile of 37.50 days. Periods of ≤ 5 days are ruled out by the MCMC fit.

To address the strong variability seen in the SPECULOOS data, several approaches were explored. The initial fit using a sinusoidal model captured some dominant periodic components, but also highlighted the quasi-periodic nature of the variability. This was further supported by an analysis using the ACF. Due to the complexity of the variability, a more flexible, non-parametric method was adopted, namely a GP. By combining an SHO and a Matern kernel, quasi-periodic variations as well as smooth long-term trends were accounted for. Through validation with injected transits into the dataset, the hyperparameters were fine-tuned and it was ensured that the model did not overfit the data and absorb transits.

The optimized GP led to a significant reduction in RMS compared to the sine model, while still maintaining sensitivity to transits. While a BLS analysis did not reveal a significant transit detection, a visual inspection of the residual flux led to the identification of 13 potentially transit-like patterns. A candidate period of 21.30

days matched 4 of these patterns and produced a consistent dip in the phase-folded light curve, however notably shallower than the original EUROPA event. A follow-up MCMC fit using this period failed to further constrain the orbital parameters.

Several limitations must be considered, as discussed in Section 4.5.6. The difference in transit shapes, and a potential misalignment of one pattern, suggest multiple possibilities: (1) the true orbital period could deviate slightly from 21.30 days, possibly due to transit timing variations (TTVs); (2) residual stellar variability or systematics may still be obscuring real transits; (3) imperfections in data reduction might have introduced subtle biases. Any combination of these factors could be responsible. It is also possible that only one or a few of the detected signals are planetary in origin, potentially arising from a multi-planet system. The initial pattern may correspond to a genuine transit, but with a different orbital period, such as those listed in Table 10. A false-positive scenario also cannot be ruled out.

Therefore, while the 21.30-day period remains plausible, it should be treated with caution. Follow-up observations and further analysis could provide valuable insights and are certainly worth pursuing.

This work also points to the broader insight, that standard tools such as BLS may not be optimal for detecting shallow transits in data exhibiting high variability. Assuming transits are indeed present, more advanced or tailored detection techniques are needed.

Looking ahead, several directions could build on this foundation. Automating the fine-tuning of GP hyperparameters using injected transits could enable broader application across multiple targets. Machine learning techniques may further enhance GP modeling, either by training on light curves from similar targets, or by automating the detection of transit-like features in residual light curves, which in this study was done visually. Additionally, radial velocity follow-up could be valuable in confirming or ruling out planetary candidates.

For the targets analyzed in this thesis, further observations represent the next logical step, based on the constraints and potential ephemerids derived here. If the signals observed are planetary in nature, there remains a real possibility of detecting them again.

References

- Agol, E., Steffen, J., Sari, R., & Clarkson, W. 2005, Monthly Notices of the Royal Astronomical Society, 359, 567, doi: [10.1111/j.1365-2966.2005.08922.x](https://doi.org/10.1111/j.1365-2966.2005.08922.x)
- Aigrain, S., Parviainen, H., & Pope, B. J. S. 2016, Monthly Notices of the Royal Astronomical Society, 459, 2408, doi: [10.1093/mnras/stw706](https://doi.org/10.1093/mnras/stw706)
- Astropy Collaboration, Price-Whelan, A. M., Lim, P. L., et al. 2022, The Astrophysical Journal, 935, 167, doi: [10.3847/1538-4357/ac7c74](https://doi.org/10.3847/1538-4357/ac7c74)
- Bell, K. J. 2020, Research Notes of the American Astronomical Society, 4, 19, doi: [10.3847/2515-5172/ab72aa](https://doi.org/10.3847/2515-5172/ab72aa)
- Borucki, W. J., Koch, D., Basri, G., et al. 2010, Science, 327, 977, doi: [10.1126/science.1185402](https://doi.org/10.1126/science.1185402)
- Bradley, L., Sipőcz, B., Robitaille, T., et al. 2024, astropy/photutils: Version 2.0.2, <https://doi.org/10.5281/zenodo.13989456>
- Collins, K. A., Kielkopf, J. F., Stassun, K. G., & Hessman, F. V. 2016, arXiv e-prints, arXiv:1601.02622, doi: [10.48550/arXiv.1601.02622](https://doi.org/10.48550/arXiv.1601.02622)
- Cushing, M. C., Kirkpatrick, J. D., Gelino, C. R., et al. 2011, The Astrophysical Journal, 743, 50, doi: [10.1088/0004-637X/743/1/50](https://doi.org/10.1088/0004-637X/743/1/50)
- Davy Kirkpatrick, J., Gelino, C. R., Cushing, M. C., et al. 2012, The Astrophysical Journal, 753, 156, doi: [10.1088/0004-637X/753/2/156](https://doi.org/10.1088/0004-637X/753/2/156)
- Delrez, L., Gillon, M., Queloz, D., et al. 2018, in Society of Photo-Optical Instrumentation Engineers (SPIE) Conference Series, Vol. 10700, Ground-based and Airborne Telescopes VII, ed. H. K. Marshall & J. Spyromilio, 107001I, doi: [10.1117/12.2312475](https://doi.org/10.1117/12.2312475)
- Demory, B. O., Pozuelos, F. J., Gómez Maqueo Chew, Y., et al. 2020, Astronomy & Astrophysics, 642, A49, doi: [10.1051/0004-6361/202038616](https://doi.org/10.1051/0004-6361/202038616)
- Dupuy, T. J., Liu, M. C., Best, W. M. J., et al. 2019, The Astronomical Journal, 158, 174, doi: [10.3847/1538-3881/ab3cd1](https://doi.org/10.3847/1538-3881/ab3cd1)
- Foreman-Mackey, D., Agol, E., Angus, R., & Ambikasaran, S. 2017, ArXiv. <https://arxiv.org/abs/1703.09710>
- Foreman-Mackey, D., Hogg, D. W., Lang, D., & Goodman, J. 2013, Publications of the Astronomical Society of the Pacific, 125, 306, doi: [10.1086/670067](https://doi.org/10.1086/670067)
- Gagné, J., Faherty, J. K., Cruz, K. L., et al. 2015, The Astrophysical Journal Supplement Series, 219, 33, doi: [10.1088/0067-0049/219/2/33](https://doi.org/10.1088/0067-0049/219/2/33)
- Garcia, L. J., Foreman-Mackey, D., Murray, C. A., et al. 2024, The Astronomical Journal, 167, 284, doi: [10.3847/1538-3881/ad3cd6](https://doi.org/10.3847/1538-3881/ad3cd6)
- Gardner, J. P., Mather, J. C., Clampin, M., et al. 2006, Space Science Reviews, 123, 485, doi: [10.1007/s11214-006-8315-7](https://doi.org/10.1007/s11214-006-8315-7)
- Gelman, A., Carlin, J., Stern, H., et al. 2013, Bayesian Data Analysis, 3rd edn. (United States: CreateSpace)

- Gelman, A., & Rubin, D. B. 1992, Statistical Science, 7, 457, doi: [10.1214/ss/1177011136](https://doi.org/10.1214/ss/1177011136)
- Gillon, M., Triaud, A. H. M. J., Jehin, E., et al. 2013, Astronomy & Astrophysics, 555, L5, doi: [10.1051/0004-6361/201321620](https://doi.org/10.1051/0004-6361/201321620)
- Gillon, M., Triaud, A. H. M. J., Demory, B.-O., et al. 2017, Nature, 542, 456, doi: [10.1038/nature21360](https://doi.org/10.1038/nature21360)
- Gómez Maqueo Chew, Y., Demory, B. O., Sabin, L., et al. 2023, in Revista Mexicana de Astronomía y Astrofísica Conference Series, Vol. 55, Revista Mexicana de Astronomía y Astrofísica Conference Series, 44–46, doi: [10.22201/ia.14052059p.2023.55.10](https://doi.org/10.22201/ia.14052059p.2023.55.10)
- Goodman, J., & Weare, J. 2010, Communications in Applied Mathematics and Computational Science, 5, 65, doi: [10.2140/camcos.2010.5.65](https://doi.org/10.2140/camcos.2010.5.65)
- Hastings, W. K. 1970, Biometrika, 57, 97. <http://www.jstor.org/stable/2334940>
- Hippke, M., & Heller, R. 2019, Astronomy & Astrophysics, 623, A39, doi: [10.1051/0004-6361/201834672](https://doi.org/10.1051/0004-6361/201834672)
- Holman, M. J., & Murray, N. W. 2005, Science, 307, 1288, doi: [10.1126/science.1107822](https://doi.org/10.1126/science.1107822)
- Howell, S. B. 2006, Handbook of CCD Astronomy, Vol. 5 (Cambridge University Press)
- Husser, T. O., Wende-von Berg, S., Dreizler, S., et al. 2013, Astronomy & Astrophysics, 553, A6, doi: [10.1051/0004-6361/201219058](https://doi.org/10.1051/0004-6361/201219058)
- Koch, D. G., Borucki, W. J., Basri, G., et al. 2010, The Astrophysical Journal Letters, 713, L79, doi: [10.1088/2041-8205/713/2/L79](https://doi.org/10.1088/2041-8205/713/2/L79)
- Kovács, G., Zucker, S., & Mazeh, T. 2002, Astronomy & Astrophysics, 391, 369, doi: [10.1051/0004-6361:20020802](https://doi.org/10.1051/0004-6361:20020802)
- Kreidberg, L. 2015, Publications of the Astronomical Society of the Pacific, 127, 1161, doi: [10.1086/683602](https://doi.org/10.1086/683602)
- Lang, D., Hogg, D. W., Mierle, K., Blanton, M., & Roweis, S. 2010, The Astronomical Journal, 137, 1782
- Lightkurve Collaboration, Cardoso, J. V. d. M., Hedges, C., et al. 2018, Lightkurve: Kepler and TESS time series analysis in Python, Astrophysics Source Code Library. <http://ascl.net/1812.013>
- Lomb, N. R. 1976, Astrophysics and Space Science, 39, 447, doi: [10.1007/BF00648343](https://doi.org/10.1007/BF00648343)
- Mamajek, E. E., Barenfeld, S. A., Ivanov, V. D., et al. 2015, The Astrophysical Journal Letters, 800, L17, doi: [10.1088/2041-8205/800/1/L17](https://doi.org/10.1088/2041-8205/800/1/L17)
- Mandel, K., & Agol, E. 2002, The Astrophysical Journal Letters, 580, L171, doi: [10.1086/345520](https://doi.org/10.1086/345520)
- Marois, C., Macintosh, B., Barman, T., et al. 2008, Science, 322, 1348, doi: [10.1126/science.1166585](https://doi.org/10.1126/science.1166585)
- Mayor, M., & Queloz, D. 1995, Nature, 378, 355, doi: [10.1038/378355a0](https://doi.org/10.1038/378355a0)
- McQuillan, A., Aigrain, S., & Mazeh, T. 2013, Monthly Notices of the Royal Astronomical Society, 432, 1203, doi: [10.1093/mnras/stt536](https://doi.org/10.1093/mnras/stt536)
- Morris, B. M., Tollerud, E., Sipőcz, B., et al. 2018, The Astronomical Journal, 155, 128, doi: [10.3847/1538-3881/aaa47e](https://doi.org/10.3847/1538-3881/aaa47e)

- Newton, E. R., Irwin, J., Charbonneau, D., et al. 2016, *The Astrophysical Journal*, 821, 93, doi: [10.3847/0004-637X/821/2/93](https://doi.org/10.3847/0004-637X/821/2/93)
- Osborn, H. P., Armstrong, D. J., Brown, D. J. A., et al. 2016, *Monthly Notices of the Royal Astronomical Society*, 457, 2273, doi: [10.1093/mnras/stw137](https://doi.org/10.1093/mnras/stw137)
- Parviainen, H., & Aigrain, S. 2015, *Monthly Notices of the Royal Astronomical Society*, 453, 3821, doi: [10.1093/mnras/stv1857](https://doi.org/10.1093/mnras/stv1857)
- Payne, M. J., & Lodato, G. 2007, *Monthly Notices of the Royal Astronomical Society*, 381, 1597, doi: [10.1111/j.1365-2966.2007.12362.x](https://doi.org/10.1111/j.1365-2966.2007.12362.x)
- Pedregosa, F., Varoquaux, G., Gramfort, A., et al. 2011, *Journal of Machine Learning Research*, 12, 2825
- Petrucci, R. P., Gómez Maqueo Chew, Y., Jofré, E., Segura, A., & Ferrero, L. V. 2024, *Monthly Notices of the Royal Astronomical Society*, 527, 8290, doi: [10.1093/mnras/stad3720](https://doi.org/10.1093/mnras/stad3720)
- Pont, F., Zucker, S., & Queloz, D. 2006, *Monthly Notices of the Royal Astronomical Society*, 373, 231, doi: [10.1111/j.1365-2966.2006.11012.x](https://doi.org/10.1111/j.1365-2966.2006.11012.x)
- Price, E. M., Rogers, L. A., Johnson, J. A., & Dawson, R. I. 2015, *The Astrophysical Journal*, 799, 17, doi: [10.1088/0004-637X/799/1/17](https://doi.org/10.1088/0004-637X/799/1/17)
- Rasmussen, C. E., & Williams, C. K. I. 2006, Gaussian Processes for Machine Learning, Adaptive Computation and Machine Learning (Cambridge, MA: MIT Press). <http://www.gaussianprocess.org/gpml/>
- Ricker, G. R., Winn, J. N., Vanderspek, R., et al. 2015, *Journal of Astronomical Telescopes, Instruments, and Systems*, 1, 014003, doi: [10.1117/1.JATIS.1.1.014003](https://doi.org/10.1117/1.JATIS.1.1.014003)
- Roberts, S., Osborne, M., Ebden, M., et al. 2013, *Philosophical Transactions of the Royal Society A: Mathematical, Physical and Engineering Sciences*, 371, 20110550, doi: [10.1098/rsta.2011.0550](https://doi.org/10.1098/rsta.2011.0550)
- Scargle, J. D. 1982, *The Astrophysical Journal*, 263, 835, doi: [10.1086/160554](https://doi.org/10.1086/160554)
- Scholz, R. D. 2014, *Astronomy & Astrophysics*, 561, A113, doi: [10.1051/0004-6361/201323015](https://doi.org/10.1051/0004-6361/201323015)
- Seabold, S., & Perktold, J. 2010, in 9th Python in Science Conference
- Seager, S., Bains, W., & Petkowski, J. 2015, in AAS/Division for Extreme Solar Systems Abstracts, Vol. 47, AAS/Division for Extreme Solar Systems Abstracts, 500.01
- Sebastian, D., Gillon, M., Ducrot, E., et al. 2021, *Astronomy & Astrophysics*, 645, A100, doi: [10.1051/0004-6361/202038827](https://doi.org/10.1051/0004-6361/202038827)
- Shumway, R. H., & Stoffer, D. S. 2020, Time Series Analysis and Its Applications, 4th edn. (New York, NY, USA: Springer), doi: [10.1007/978-3-030-62470-3](https://doi.org/10.1007/978-3-030-62470-3)
- Skrutskie, M. F., Cutri, R. M., Stiening, R., et al. 2006, *The Astronomical Journal*, 131, 1163, doi: [10.1086/498708](https://doi.org/10.1086/498708)
- Street, R. A., Fulton, B. J., Scholz, A., et al. 2015, *The Astrophysical Journal*, 812, 161, doi: [10.1088/0004-637X/812/2/161](https://doi.org/10.1088/0004-637X/812/2/161)

Sybilski, P., Konacki, M., & Kozowski, S. 2010, Monthly Notices of the Royal Astronomical Society, 405, 657, doi: [10.1111/j.1365-2966.2010.16490.x](https://doi.org/10.1111/j.1365-2966.2010.16490.x)

VanderPlas, J. T. 2018, The Astrophysical Journal Supplement Series, 236, 16, doi: [10.3847/1538-4365/aab766](https://doi.org/10.3847/1538-4365/aab766)

Vats, D., & Knudson, C. 2018, arXiv e-prints, arXiv:1812.09384, doi: [10.48550/arXiv.1812.09384](https://doi.org/10.48550/arXiv.1812.09384)

Wang, Y.-F., Luo, A. L., Chen, W.-P., et al. 2022, Astronomy & Astrophysics, 660, A38, doi: [10.1051/0004-6361/202142009](https://doi.org/10.1051/0004-6361/202142009)

Winn, J. N. 2010, in Exoplanets, ed. S. Seager (University of Arizona Press), 55–77, doi: [10.48550/arXiv.1001.2010](https://doi.org/10.48550/arXiv.1001.2010)

Winn, J. N., & Fabrycky, D. C. 2015, Annual Review of Astronomy and Astrophysics, 53, 409, doi: [10.1146/annurev-astro-082214-122246](https://doi.org/10.1146/annurev-astro-082214-122246)

York, D. G., Adelman, J., Anderson, Jr., J. E., et al. 2000, The Astronomical Journal, 120, 1579, doi: [10.1086/301513](https://doi.org/10.1086/301513)

A TESS analysis of SP1036+1923

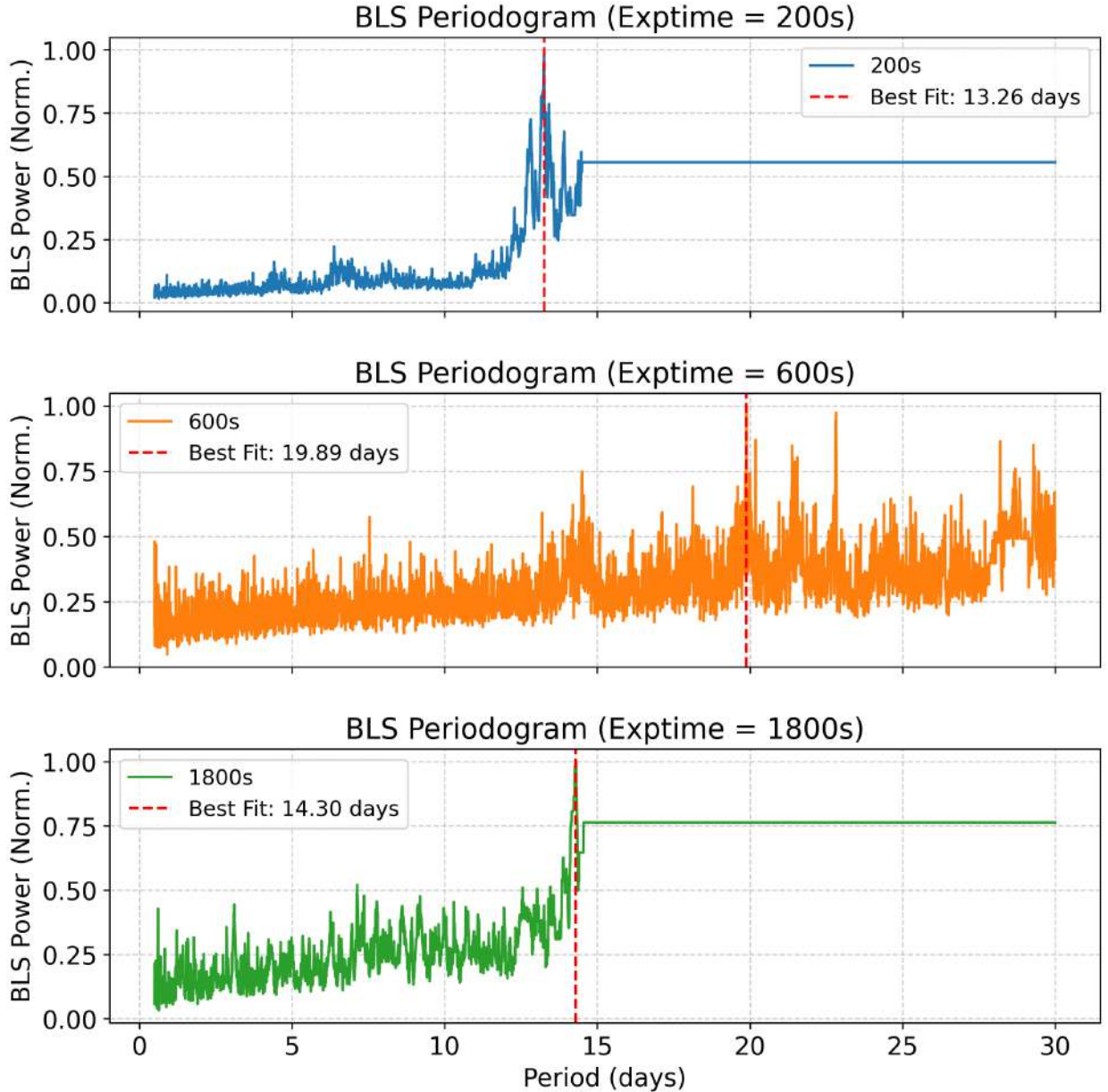


Figure 40: TESS data of SP1036+1923: Box Least Squares (BLS) periodograms for exposure times of 200 seconds, 600 seconds, and 1800 seconds. Each panel shows the normalized power spectrum (black) with the best-fit period indicated by the red dashed line. The vertical axis shows relative power (normalized to maximum).

B Python Code Setup for GP Modeling

```

import numpy as np
import celerite
from celerite import terms
import emcee

# Define composite kernel: SHO + Matern-3/2
sho_kernel = terms.SHOTerm(log_S0=np.log(S0), log_Q=np.log(Q), log_omega0=np.log(w0))
matern_kernel = terms.Matern32Term(log_sigma=np.log(sigma), log_rho=np.log(rho))
combined_kernel = sho_kernel + matern_kernel

# Define log-likelihood
def log_likelihood(params, time, flux, flux_err):
    log_S0, log_Q, log_omega0, log_sigma, log_rho = params
    kernel = terms.SHOTerm(log_S0, log_Q, log_omega0) + terms.Matern32Term(log_sigma,
        log_rho)
    gp = celerite.GP(kernel)
    gp.compute(time, flux_err)
    return gp.log_likelihood(flux)

# Define log-prior
def log_prior(params):
    # Log-normal priors within bounds (not shown numerically here)
    return logp_S0 + logp_Q + logp_omega0 + logp_sigma + logp_rho

# Define log-posterior
def log_posterior(params, time, flux, flux_err):
    lp = log_prior(params)
    if not np.isfinite(lp):
        return -np.inf
    return lp + log_likelihood(params, time, flux, flux_err)

# Set up MCMC sampler
initial = np.array([np.log(S0), np.log(Q), np.log(w0), np.log(sigma), np.log(rho)])
initial_pos = initial + 1e-4 * np.random.randn(n_walkers, len(initial))
sampler = emcee.EnsembleSampler(n_walkers, len(initial), log_posterior, args=(time, flux,
    flux_err))

# Run MCMC
sampler.run_mcmc(initial_pos, n_steps, progress=True)
samples = sampler.get_chain(discard=burnin, thin=thin, flat=True)

```

C Transit-Like Residuals Inspection

The GP-modeled residuals (Section 4.5) show 13 visually identified transit-like events. These are shown in Figure 41, with candidate mid-transit times marked. Figures 42 and 43 display the residuals around the predicted transit times for the candidate periods of 10.65 and 7.10 days.

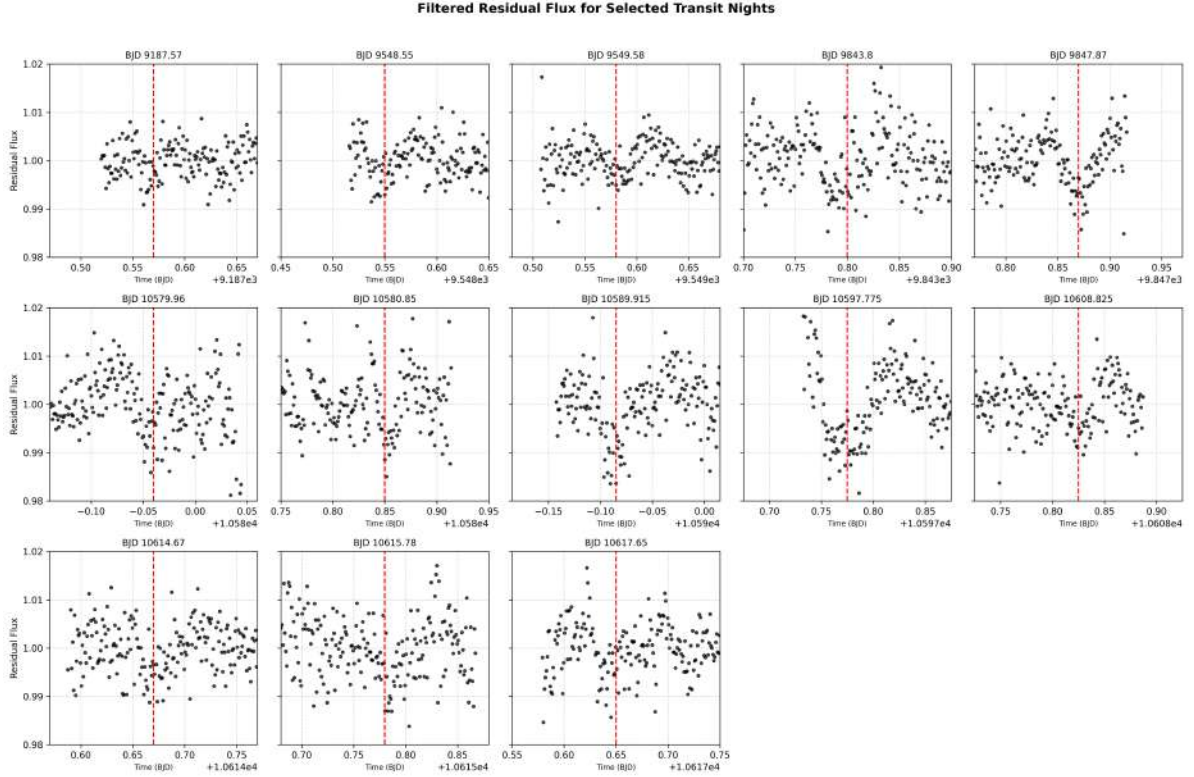


Figure 41: Residual flux measurements for the 13 selected transit-like patterns. The red dashed line marks the potential transit mid-time for each night.

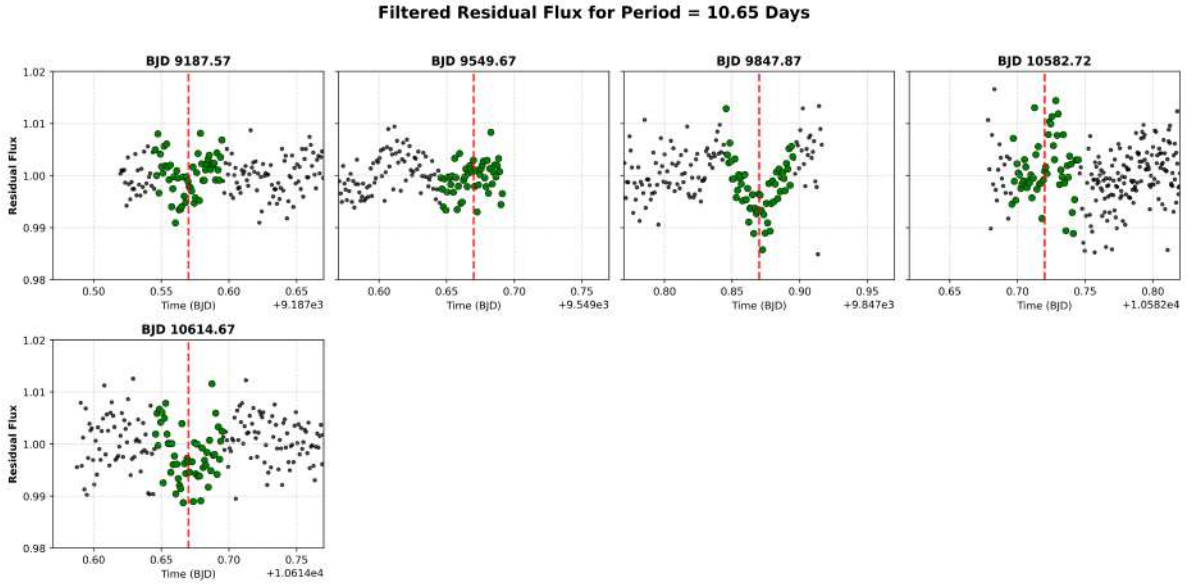


Figure 42: Residual flux around predicted transits for $t_0 = 9847.87$ BJD and $P = 10.65$ days.

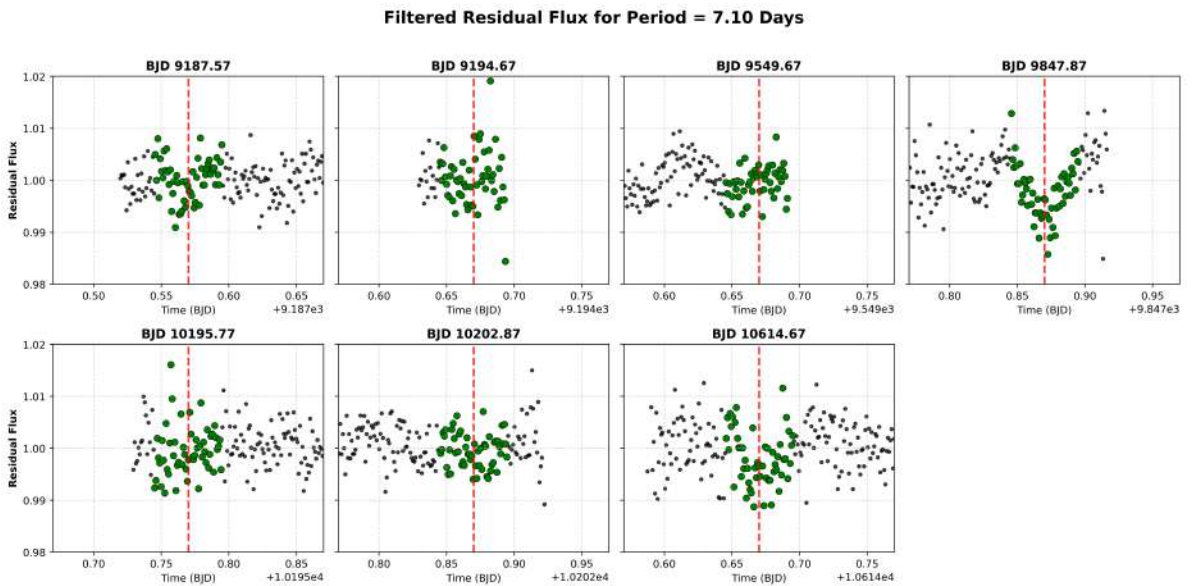


Figure 43: Residual flux around predicted transits for $t_0 = 9847.87$ BJD and $P = 7.10$ days.

Declaration of consent

on the basis of Article 30 of the RSL Phil.-nat. 18

Name/First Name: Schmid Yanick

Registration Number: 16-119-224

Study program: Experimental Physics, Applied Physics, Astronomy

Bachelor

Master

Dissertation

Title of the thesis: Hunting Transit Patterns: A Search for Exoplanets Around Ultracool Stars

Supervisor: Prof. Dr. Brice-Olivier Demory

I declare herewith that this thesis is my own work and that I have not used any sources other than those stated. I have indicated the adoption of quotations as well as thoughts taken from other authors as such in the thesis. I am aware that the Senate pursuant to Article 36 paragraph 1 litera r of the University Act of 5 September, 1996 is authorized to revoke the title awarded on the basis of this thesis.

For the purposes of evaluation and verification of compliance with the declaration of originality and the regulations governing plagiarism, I hereby grant the University of Bern the right to process my personal data and to perform the acts of use this requires, in particular, to reproduce the written thesis and to store it permanently in a database, and to use said database, or to make said database available, to enable comparison with future theses submitted by others.

Bern, 14.04.2025

Place/Date



Signature